IOWA STATE UNIVERSITY
Digital Repository

2004

Theoretical and experimental explorations in atomic force microscopy

Anil Gannepalli
Iowa State University

NOTE TO USERS

Theoretical and experimental explorations in atomic force microscopy

by

Anil Gannepalli

A dissertation submitted to the graduate faculty

in partial fulfillment of the requirements for the degree of

DOCTOR OF PHILOSOPHY

Co-majors: Chemical Engineering; Electrical Engineering

Program of Study Committee:
Surya K. Mallapragada, Co-major Professor
Murti V. Salapaka, Co-major Professor
Richard C. Seagrave
Vijay Vittal
Balaji Narasimhan

Iowa State University

Ames, Iowa

2004

UMI Number: 3136312

INFORMATION TO USERS

The quality of this reproduction is dependent upon the quality of the copy submitted. Broken or indistinct print, colored or poor quality illustrations and photographs, print bleed-through, substandard margins, and improper alignment can adversely affect reproduction.

In the unlikely event that the author did not send a complete manuscript and there are missing pages, these will be noted. Also, if unauthorized copyright material had to be removed, a note will indicate the deletion.

UMI®

Graduate College
Iowa State University

This is to certify that the Doctoral dissertation of

Anil Gannepalli

has met the dissertation requirements of Iowa State University

Signature was redacted for privacy.

Co-major Professor

Signature was redacted for privacy.

Co-major Professor

Signature was redacted for privacy.

For the Co-major Program

Signature was redacted for privacy.

For the Co-major Program

DEDICATION

To my parents and sister

and

the memory of Dr. S. P. Sengupta

ACKNOWLEDGMENTS

Life in graduate school is defined, largely, by the advisor(s) and friends one has. Considering that I have spent a good part of my life in graduate school, I'm very fortunate to have been in the company of the best people I could ever wish for.

Dr. Surya Mallapragada took me in as her first doctoral student and I was allowed the complete freedom to pursue my research interests. For that and her assurance in me, I am extremely grateful.

Dr. Murti Salapaka has been an advisor and friend in my last three years of my graduate education. I'm indebted to him for teaching me much, much more than just Modern Control Theory.

Eight years is a long time and friends make it seem go by in an instant. There are too many names to list, but they are too dear to forget. I am ever thankful for their friendship and they will always be in my thoughts.

My stay at Iowa State would not have been as pleasant without the friendly and efficient staff in the Department of Chemical Engineering.

I express my gratitude to the scientific community "out there" who have been most generous with their time, effort and intellect for all the questions I had during the course of my Ph.D.

I would not have been here today without the inspiration of Dr. S. P. Sengupta – my mentor and teacher in undergrad.

Most of all, I would like to thank my parents and sister for their love and absolute confidence in me.

TABLE OF CONTENTS

ABSTRACT

Nanotechnology is the capability to build by controlling the arrangement of individual atoms and molecules. Such a technology would be founded on the ability to *control, manipulate* and *investigate* matter at the atomic scale. The invention of atomic force microscope (AFM) and the advances in micro-cantilever based scanning probe technology have significantly enhanced the experimental capability to probe and modify matter at the nanoscale. However, it is still severely limited in achieving the necessary bandwidth, sensitivity and resolution. To further the advances in this field an in-depth understanding of the nature and effects of the tip-sample interactions is imperative. A complementary approach involving theoretical investigations and experimental advances is best suited to overcome the current limitations of this technology.

This thesis investigates the atomistic phenomena associated with material modification at the tip-sample contact theoretically because such information is inaccessible to experimental observation. Molecular dynamics studies of nanoindentation of crystalline silicon and gold, representative of semi-conductor and metallic substrates, shed light on the mechanics of plastic deformation and defect forma-tion. Silicon undergoes a densification transformation to amorphous phase in the deformed region via the formation of interstitials. In gold a pyramidal defect structure is formed via a three step mechanism consisting of nucleation, glide and reaction of dislocations. This mechanism dictates the dependence of defect structure on the crystallography of the indented surface as observed in experimental studies performed by other researchers.

The experimental studies develop a new small amplitude non-contact AFM technique. In this frequency modulation method, changes in the cantilever's resonance induced by the tip-sample inter-actions are detected from its thermal noise response. By eliminating the need for positive feedback it enables maintaining an extremely small tip-sample separation for extended periods of time at room

temperatures. Consequently, this technique is particularly suited for studying highly localized slowly evolving atomic or molecular scale phenomena at ambient temperatures. The experiments performed in ambient room conditions have achieved tip-sample separations less than 2 nm for time periods in excess of 30 min. At such small separations a narrowband signal at 250 Hz is imaged with a force sensitivity of 14 fN in a bandwidth of 0.4 Hz.

CHAPTER 1   INTRODUCTION

1.1   Nanotechnology

Four decades have passed since Richard Feynman, Nobel Laureate in Physics, delivered his prophetic talk *There is plenty of room at the bottom* [1]. In it he addressed the "problem of manipulating and controlling things on a small scale" and concluded with a note on "the possibility of maneuvering things atom by atom" without violating the principles of physics. This capability to control the arrangement of atoms is the essence of *Nanotechnology* and is one of the ultimate challenges of science and technology. Such a technology would be founded on, of other things, three basic capabilities - the ability to *control, manipulate* and *investigate* matter at the atomic scale. This would require a device that can achieve positional and temporal control on the order of, or better than, the length and time scales of atomistic phenomena. Such a device must also be capable of imparting forces that are small and localized enough to affect a single atom. Finally, the device must be able to detect the changes in the locale of an atom. In effect, the device must have extremely high *bandwidth, resolution* and *sensitivity*.

Since the classic talk there has been significant progress towards the realization of Feynman's dream. The single most significant advance is the invention of the scanning probe microscopes (SPM), of which the micro-cantilever based atomic force microscope (AFM) [2] has been the most popular. These devices have a demonstrated capability to not only image at the atomic scale, but also manipulate materials and probe material properties at the nanoscale. This makes them an ideal tool for Nanotechnology.

1.2 Motivation

A significant impact of this new found capability is in the area of microfabrication, which is continually being refined to achieve smaller feature sizes and move from submicron lengths to nanoscales. These micro-cantilever based devices have the potential to have a tremendous impact in biosystems [3]. They have been shown to assist in a better understanding of the interface between the surface and biomolecules, and cells and membranes. A molecular level understanding of surface adhesion [4], surface interactions [5] and biomolecular recognition [6] have been demonstrated with these devices. Such an understanding is the basis for the development of novel diagnostic and therapeutic devices by exploiting the inherent capabilities of biological cells — *cellular* and *tissue engineering*. The high sensitivity and resolution of AFM have enabled mechanical detection of magnetic resonance [7, 8] and rapid advances in force detection sensitivity have the potential to achieve the detection of single electron spin [9]. Single electron spin readout is the key requirement in the solid state implementation of a quantum computer, which due to its inherently exponential parallelism will far exceed the capabilities of existing and future conventional computers. These are but a few examples where micro-cantilever based devices have made a significant impact and the reader is referred elsewhere [10] for more information.

Despite the promise this technology holds, it is severely limited in its current state of the art. Central to the operation of these devices is the nature of the tip-sample interactions and their effect on the cantilever and the sample. An in-depth understanding of these issues will shed light on ways to overcome the current limitations.

In particular, knowledge of the manner in which the tip effects the sample during modification will shed light on the capabilities and limitations of the tip based nanofabrication. Towards this effort, the current study focusses on gaining insights into material behavior at atomic scales when the sample is being indented by the AFM tip. Such studies are inaccessible to experimental observation and molecular dynamics (MD) simulations, by virtue of their high temporal and spatial resolution, offer an ideal approach to study atomic-scale processes and understand their mechanisms.

The micro-cantilever acts as the sensor to detect the tip-sample interactions. Investigating the manner in which the tip-sample interactions effect the dynamics of the cantilever is crucial to extend the

current capabilities of AFM technology. The thermal noise response of the cantilever to the tip-sample forces is studied and the insight gained is used to develop a new small amplitude frequency modulation (FM) non-contact AFM technique. In contrast to the exiting FM techniques, this method eliminates the use of a driven cantilever and positive feedback. This allows for extremely small tip-sample separations resulting in enhanced force detection sensitivity at room temperatures.

1.3 Organization

This thesis is organized into 6 chapters. Chapter 1 provides an introduction to this study and the motivation behind it. Chapter 2 deals with the essentials of the scanning probe microscopy, particularly the AFM and provides a brief background on molecular dynamics technique. Chapters 3 and 4 present the molecular dynamics studies of the nanoindentation of crystalline silicon (Si(001)) and gold (Au(001)) substrates, respectively. Chapter 5 develops the new thermal noise based non-contact AFM imaging technique. Conclusions and directions for future work are presented in Chapter 6.

CHAPTER 2 BACKGROUND

2.1 Scanning Probe Microscopy

The invention of the scanning tunneling microscope (STM) in 1981 by Binning and Rohrer [11] lead to the imaging of individual atoms for the very first time. This invention won them Nobel Prize in Physics in 1986 and lead to the development of a series of novel scanning probe microscopes (SPM) that make use of various interatomic interactions as their basis. Atomic force microscope (AFM) [2] is the second of the class of SPMs demonstrating atomic resolution [12] that has revolutionized the area of near field microscopy and opened a vast frontier of applications. Microscopy refers to the visualization of a small object and is typically carried out by using a suitable probe, measuring an appropriate signal followed by image construction from the measured signal. In traditional microscopes using a wave probe, the construction of the image is limited by diffraction and the best resolution possible is one half the probe wavelength. Scanning probe microscopes have no such limit because the measurement involves highly local interactions between the probe and the sample, which are separated by a few Å to nanometers. Imaging is done by moving the probe across the surface and measuring the variations in the signal. The resolution is determined by the size of the probe, the locality of the interaction and the probe-sample separation. In an STM a biased sharp tip, acting as the probe, is brought close to the sample resulting in a tunneling current between the tip and the sample. This current has an exponential dependence on the tip-sample separation resulting in atomic resolution of the STM. However, STM has a serious limitation because it requires a conducting sample to facilitate the tunneling current.

AFM utilizes the interatomic interaction forces that are universal, and therefore has no such limitation. The versatility of AFM to operate under varied conditions, *eg.*, air [12], solution [13] and vacuum [14] with high resolution is one of its main advantages.

2.2 Atomic Force Microscope

A brief description of the operation of the AFM, instrumentation and operating modes is given below. For detailed description and analysis the reader is referred elsewhere [15, 16, 17].
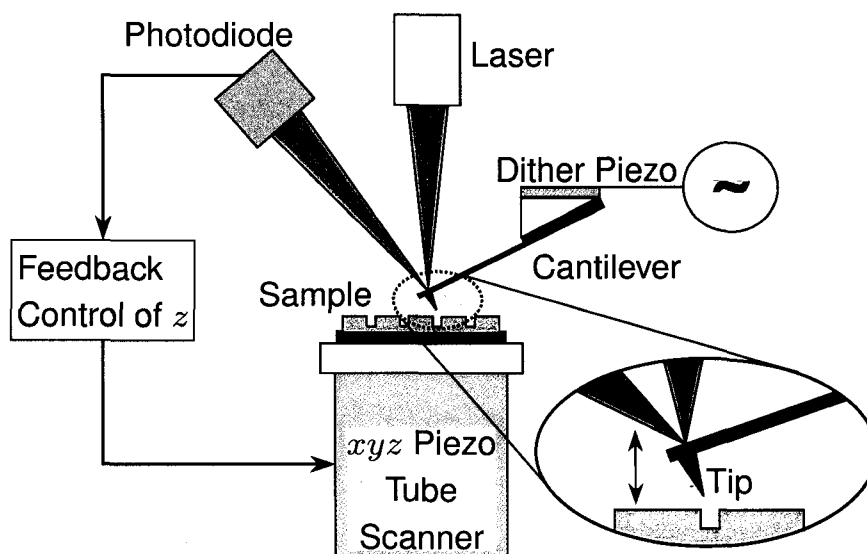
Figure 2.1 Schematic of the instrumentation of a basic AFM.

2.2.1 Basic Operating Principles

Schematic of a typical AFM is illustrated in Figure 2.1. AFM uses the interatomic forces that exist between atoms and molecules. During operation the tip mounted on a cantilever is brought very close to the sample, so that the tip atoms interact with the atoms of the sample. These interaction forces effect the cantilever and the changes in either the static deflection or its dynamic properties are measured to extract the image.

There are two regimes of force that the tip experiences while scanning close to the sample surface. The distance dependent tip-sample forces, depicted in Figure 2.2, consist of short-range and long-range forces specific to the tip-sample system. Short-range forces comprise the chemical forces with a range less than a nanometer. These forces are mildly attractive but immensely repulsive at small separations. The long-range forces include the van der Waals, magnetic and electrostatic forces with an interaction range up to 100 nm. The van der Waals forces are ubiquitous and are always attractive making the

Figure 2.2 (a) Repulsive and attractive force regimes present in the tip-sample attraction. Different modes explore different force regimes. Static – repulsive; tapping – attractive and repulsive; non-contact – attractive. (b) In static mode the cantilever is effected by three forces: 1. repulsive short-range forces a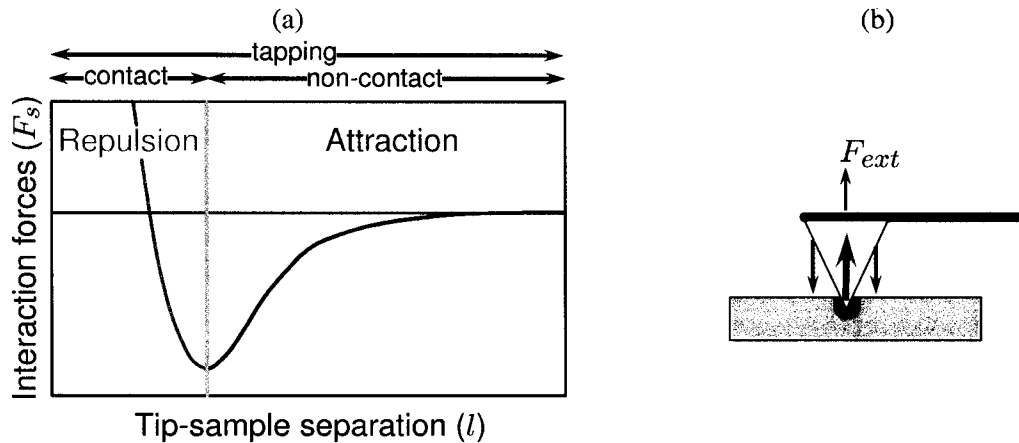t tip-sample contact, 2. attractive forces acting on the part of the tip not in contact, and 3. external force applied during imaging. A combination of these forces results in a finite tip-sample contact area of about 1–10 nm in size.

typical long-range forces attractive. In ambient conditions capillary and adhesion forces come into play due to the adsorption of water and other molecules on the sample surface.

The short-range forces are a consequence of the overlap of electron clouds and ionic repulsion. The variation of these forces on the atomic scale leads to atomic resolution in AFM. For very small separations, the short-range forces will be dominant and almost all the information is contributed by the sample atoms closest to the tip resulting in atomic resolution. At large separations, the long-range forces dominate and the resolution deteriorates due to the many-atom interaction between the tip and the sample.

2.2.2 Instrumentation

A typical AFM consists of a force sensor, sample positioning system, detection system and a control system. The tip interacting with the sample is mounted on the end of a micro-cantilever which acts as the force sensor. The choice of a cantilever for a particular application is dictated by the stiffness k, resonant frequency ω_R, the quality factor Q, thermal drift of the resonance $\partial\omega_R/\partial T$ and material of

construction. A small dither-piezo is used to oscillate the cantilever for dynamic mode operation. A piezoelectric scanner or a nanopositioning stage is used to move the sample relative to the tip in a lateral direction. The deflection of the cantilever in the z direction, in most cases, is detected by an optical lever method [18]. In this scheme, shown in Figure 2.1, the light from a laser diode is reflected off the back of the cantilever to a position-sensitive photodiode that can sense the change in the reflectance angle caused by cantilever deflection. Other detection techniques employed are optical laser interferometry [19, 20] and piezoresistive cantilevers [21]. The measured deflection signal is fed to the feedback controller that effects the tip-sample interactions by moving the sample in the z direction.

2.2.3 Modes of Operation

The operational modes of the AFM are classified into static and dynamic modes depending on the nature of the measured signal. These modes are further classified based on the force regimes in which the AFM operates.

2.2.3.1 Static mode
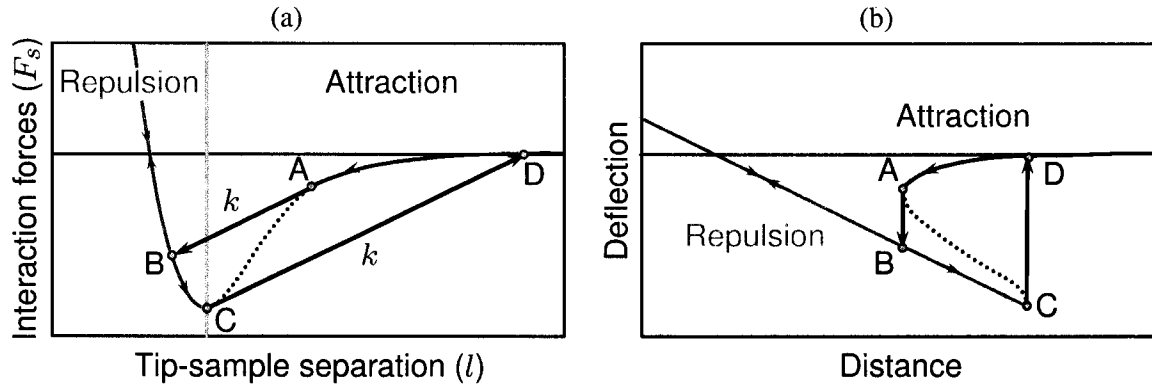
Figure 2.3 (a) Force versus distance trajectory of a cantilever undergoing jump-to-contact. During approach when $\partial F_s/\partial l > k$, a mechanical instability results in a discontinuous jump-to-contact from A to B. On retraction a sufficiently large force is required to overcome adhesion and jump out-of-contact from C to D. (b) The deflection versus distance curve corresponding to the force curve in (a). The dotted line depicts the unstable region.

In the static mode of operation, the tip-sample forces are sensed by measuring the static deflection

of the cantilever. Thus a good force detection sensitivity and non-destructive imaging necessitates the use of soft (k = 0.01 - 1 N/m) cantilevers.

Contact mode is a static mode in which the tip is in contact with the sample, therefore interacting with the sample in the repulsive regime of the interactions (see Figure 2.2). In this mode the tip-sample separation is controlled by maintaining a constant deflection of the cantilever thereby recording a constant force (F_{ext}) surface. Measurement of deflection suffers from the $1/f$ noise (see Figure 2.4) and the drift in the system induced by the changes in the surrounding environment. The drift effects are due to unpredictable changes in the deflection detector [18, 22], thermal bending [23, 24] and creep in the piezo based sample positioner. These noise and disturbance effects can be minimized in a controlled environment at low temperatures. However, force measurement in static mode at low frequencies is a considerable challenge at ambient temperatures.
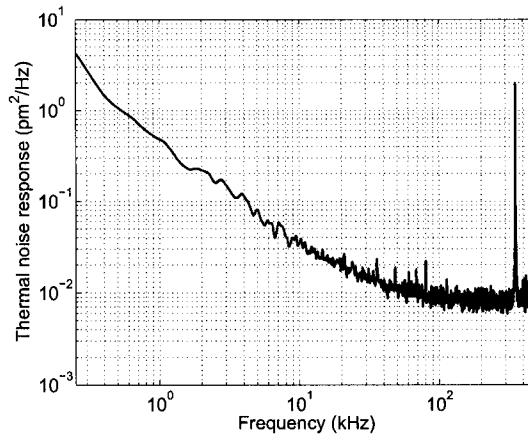
Figure 2.4 Power spectral density of a typical cantilever. At low frequencies the noise has a $1/f$ dependence and is commonly referred to as $1/f$ noise. This noise along with drift pose a considerable challenge in measuring static deflection at low frequencies in ambient conditions. The peak in the spectrum corresponds to cantilever's resonance at ω_R. In dynamic AFM a cantilever with a high resonant frequency is chosen such that the $1/f$ noise is negligible.

As depicted in Figure 2.2(b) the cantilever experiences the long-range, short-range and externally applied forces. An interplay of these forces results in a repulsive tip-sample contact with a finite size on the order of 1 − 10 nm. Consequently, the tip exerts both vertical and lateral forces on the sample causing deformation and drag that is particularly detrimental for soft samples. Furthermore, contribu-

tion of long-range forces reduce the sensitivity to the highly localized short-range forces. This reduced sensitivity to short-range forces and the finite contact area severely limit the true atomic resolution capability of contact mode.

A typical contact mode operation employing soft cantilevers is associated with the jump-to-contact instability illustrated in Figure 2.3. As the tip gets closer to the sample, a mechanical instability occurs when the gradient of the attractive force exceeds the cantilever spring constant ($\partial F_s / \partial l > k$ [25, 26]). At this point the tip jumps to contact from A to B as shown in Figure 2.3. The tip-sample force and the resulting force curve are depicted in Figures 2.3(a) and (b) respectively. During retraction, the adhesion force between the tip and sample gives rise to hysteresis seen in the force curve. A sufficiently large force is required to overcome the adhesive forces and jump out-of-contact from C to D.

2.2.3.2 Dynamic mode

(a)   (b)
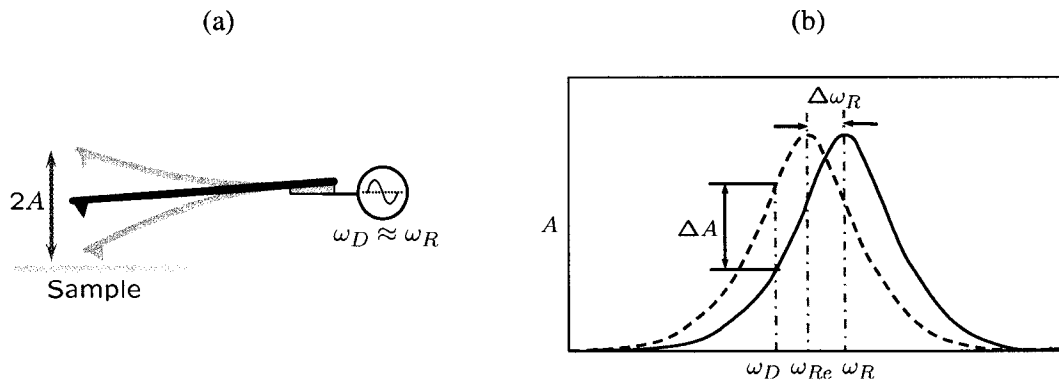
Figure 2.5   (a) In dynamic mode AFM the cantilever is oscillated at or close to its resonant frequency ($\omega_D \approx \omega_R$) (b) As the tip interacts with the sample the cantilevers resonant frequency changes. For attractive forces the resonant frequency decreases and it increases for repulsive tip-sample interactions.

In the dynamic operation mode operation, the cantilever is externally excited at or close to its resonant frequency (see Figure 2.5(a)) and the changes in the oscillation properties due to the tip-sample forces are detected. The tip-sample forces change the resonant frequency of the cantilever thereby effecting the oscillation properties as seen in Figure 2.5(b). In the absence of significant damping the changes in the resonance are primarily due to the tip-sample force gradient. Thus, unlike static mode,

dynamic mode detects the force gradient rather than the force. Dynamic AFM overcomes the detrimental effects of the $1/f$ noise and instrument drift by measuring a dynamic signal with a frequency ($\approx \omega_R$) significantly removed from low frequencies (see Figure 2.4).

In dynamic mode either the changes in amplitude and phase (*amplitude-modulation*: AM-AFM) or frequency (*frequency-modulation*: FM-AFM) can be monitored. In AM-AFM [27], the cantilever is driven by a fixed amplitude drive signal at a fixed frequency ω_D close to ω_R and the changes in amplitude and phase are fed back for controlling the tip-sample separation. In this mode however, the time constants associated with the dynamics of the cantilever amplitude are large ($\tau_{AM} \approx Q/\omega_R$) in vacuum, resulting in low bandwidths. This drawback is alleviated in FM-AFM [28], where the cantilever is oscillated at its resonant frequency at all times. A positive feedback of the of the cantilever motion as the driving signal serves to keep the cantilever at resonance. The changes in the resonance constitute the feedback signal used for imaging. These changes occur in one cycle ($\tau_{FM} \approx 1/\omega_R$) giving rise to high bandwidths. Operation in ultra-high vacuum is needed for high Q which improves the signal-to-noise ratios in frequency measurement. In dynamic mode jump-to-contact and instability due to near surface damping is avoided by the use of large oscillation amplitudes and/or stiffer cantilevers [29].

Tapping mode [30] refers to the AM mode operation where the cantilever explores both the attractive and repulsive force regimes where the tip contacts the sample at one extreme of the oscillation. Atomic resolution on silicon in vacuum has been demonstrated [31] in this mode. A significant advantage of this method is that the vertical forces on the sample are small and lateral forces are virtually eliminated. This makes tapping mode very attractive for imaging soft samples, particularly biological samples [32, 33] with good resolution. Eventhough both AM and FM can be used in *non-contact* mode, FM has gained favor due to its superior bandwidth. In non-contact (NC) mode the tip explores only the attractive regime of the tip-sample interactions thereby making this mode virtually non-destructive. This technique yielded the first true atomic resolution images [34]. However, akin to static AFM in classic NC-AFM, where the amplitude of the cantilever is large ($A \approx 10$ nm), the long-range force contributions serve to reduce the short-range force sensitivity thereby limiting the resolution. Moreover, large amplitudes result in a complex nonlinear functional dependence of the frequency shifts on

the tip-sample forces [35, 36]. Consequently, the interpretation of the data is involved and requires a deconvolution procedure [37].

The above issues are resolved by using smaller amplitudes. Amplitudes on the order of the short-range chemical force interaction lengths (≈ 1 Å) are recommended for optimal resolution [38]. Small amplitude methods require stiffer cantilevers to avoid the jump-to-contact instability and low temperature operation is necessary in current FM methods to suppress the thermal fluctuations of the cantilever. A suitable choice of cantilever spring constant k and oscillation amplitude in vacuum have resulted in atomic resolution [34, 39] rivaling that of an STM. A sub-resonance small amplitude AM technique has been recently developed [40, 41] that can be used in liquids [42]. In chapter 5 a new small amplitude FM technique based on thermal noise is developed that is particularly suitable for studying highly localized slowly evolving atomic or molecular phenomena at ambient temperatures.

In addition to the steady state modes of operation mentioned above, a new transient force microscopy (TFM) [43] has been proposed recently. In this AM technique the transients of the changes in amplitude are detected in a few oscillation cycles resulting in bandwidths independent of Q as in FM-AFM.

2.3 Molecular Dynamics Simulations

Much of the experimental research on material modification with proximal probes has been analytic in nature. The observation of particular phenomenon has been explained as the result of certain actions with the probe. With the advances in scanning probe technology it has been possible to experimentally probe material properties and phenomena at the nanoscale [44, 45, 46]. However the basic underlying atomistic mechanisms are still inaccessible to experimental observation. Molecular simulation, by virtue of its extremely high temporal and spatial resolution, offers an ideal approach to gain insights into atomic-scale processes and understand their mechanisms.

2.3.1 Molecular Modeling and Dynamics

Molecular modeling, as the name suggests deals with ways to mimic the behavior of molecules and molecular systems. Molecular dynamics (MD) mimics the evolution of the molecular system with time,

thus giving access to the dynamics of atomic processes. A realistic model of the system is crucial for the accuracy of any computer simulation. However, to keep the computational requirements manageable, approximations are made in modeling the system of interest. The concept of *potential energy surface* (PES) is one such approximation that is fundamental for modeling molecular structure and dynamics. A brief overview of the essence of the methodology is presented. A detailed discussion of the molecular simulation techniques can be found elsewhere [47, 48, 49].

2.3.1.1 Potential energy surface - The Born-Oppenheimer approximation

The flow of energy in a system dictates the manner in which it will evolve. For a molecular system the potential energy is described by the PES in terms of the positions of atomic nuclei and electrons. An exact description of these positions is given by Schrödinger's wave functions as probability distribution functions. Since, for most part, such detail is intractable and unnecessary, MD technique exploits the Born-Oppenheimer approximation. The Born-Oppenheimer approximation assumes a timescale separation of the motion of nuclei and electrons. The electronic motion is assumed to adjust to the ground state without delay, and therefore the ground state potential energy can be described as a function of the nuclear positions. This approximation is not valid when the nuclear kinetic energies are high, but under normal conditions it gives a sufficiently accurate account of molecular behavior. In order to calculate the PES, there are accurate but computationally expensive *ab-initio* methods and empirical but more workable molecular mechanics methods.

2.3.1.2 Molecular mechanics and classical molecular dynamics

Molecular mechanics makes use of the concept of chemical bond and approximates the PES in terms of bonded and non-bonded interactions. The total potential energy is treated as a sum of the potentials contributed by the constituting interactions, also known as *force field*. Therefore the PES is described as

$$V(r^N) = \sum (v_1 + v_2 + v_3 + v_4 + \cdots + v_n). \tag{2.1}$$

where $V(r^N)$ is the total potential energy which is a function of the positions r of N atoms or molecules. v_1 is the contribution due to external forces. v_2, v_3, v_4 and v_n are the contributions

due to 2-body, 3-body, 4-body and n-body bonded and non-bonded interactions. More sophisticated force fields have more terms depending on the intended application and accuracy. The parameters and functional forms are empirically derived from experimentally measured geometries, energies and vibrational spectra.

Classical molecular dynamics assumes the applicability of classical mechanics to the constituent particle experiencing the forces described by the force field. The instantaneous force F_i on a particle i is evaluated as,

$$F_i = -\nabla_{r_i} V(r^N). \tag{2.2}$$

and the successive configurations are obtained by integrating the differential equation embodied in Newton's second law of motion given below,

$$\frac{\partial^2 r_i}{\partial t^2} = \frac{F_i}{m_i}. \tag{2.3}$$

where m_i is the mass of particle i and r_i its position. The integration timestep should be chosen such that it is smaller than the timescale of atomic motion.

2.3.2 Nanoindentation Simulations

The computational model comprises tip and sample as two separate but interacting molecular systems where the Hamiltonian H of the system is given by,

$$H(r_S, r_T) \quad = \quad V(r_S, r_T) + E_{kin} \tag{2.4a}$$

$$V(r_S, r_T) \quad = \quad V_S(r_S) + V_T(r_T) + V_{TS}(r_S, r_T) \tag{2.4b}$$

$$E_{kin} \quad = \quad \sum (p_i \cdot p_i)/(2m_i). \tag{2.4c}$$

where r_S and r_T are the positions of the sample and tip atoms respectively. V_S, V_T and V_{TS} are the force fields describing the interactions between the sample atoms, tip atoms and tip-sample interactions. E_{kin} is the total kinetic energy calculated from the momenta p_i of the atoms. The equation of motion in terms of the Hamiltonian is given by

$$\dot{p}_i \quad = \quad -\frac{\partial H}{\partial r_i}, \tag{2.5a}$$

$$\dot{r}_i \quad = \quad \frac{\partial H}{\partial p_i} \tag{2.5b}$$

Silicon and gold have been chosen as representatives of semiconductor and metallic systems to study the atomistic dynamics during nanoindentation. Stillinger-Weber potential [50] is used to simulate the behavior of silicon substrate. This potential has two and three-atom contributions given by

$$
v_2(r_{ij}) = \begin{cases} \epsilon A \left[B \left(\frac{r_{ij}}{\rho}\right)^{-p} - \left(\frac{r_{ij}}{\rho}\right)^{-q} \right] \exp\left[\left(\frac{r_{ij}}{\rho} - a\right)^{-1} \right], & r_{ij} < a\rho \\ 0, & r_{ij} \geq a\rho \end{cases}
\tag{2.6a}
$$

$$
v_3(r_i, r_i, r_i) = \epsilon[h(r_{ij}, r_{ik}, \theta_{jik}) + h(r_{ji}, r_{jk}, \theta_{kji}) + h(r_{ki}, r_{kj}, \theta_{ikj})],
\tag{2.6b}
$$

with

$$
h(r_{ij}, r_{ik}, \theta_{jik}) = \begin{cases} \lambda exp\left[\gamma \left(\frac{r_{ij}}{\rho} - a\right)^{-1} + \gamma \left(\frac{r_{jk}}{\rho} - a\right)^{-1} \right] (\cos\theta_{jik} + 1/3)^2, & r_{ij}, r_{jk} < a\rho \\ 0, & r_{ij}, r_{jk} \geq a\rho \end{cases}
\tag{2.6c}
$$

where j, k are the any two nearest neighbors of atom i, $r_{ij} = |r_i - r_j|$ and ϵ is an energy parameter. v_2 and v_3 vanish at the cut-off radius ρ without any discontinuities and the tetrahedral geometry is favored by the $(\cos\theta_{jik} + 1/3)^2$ term. Stillinger and Weber found the following parametric set in optimal agreement with the experimental data:

$$
A = 7.049556277, \ p = 4, \ \gamma = 1.2,
$$

$$
B = 0.6022245584, \ q = 0, \ \lambda = 21.0,
\tag{2.7}
$$

$$
\epsilon = 3.4723 \text{ aJ}, \ a = 1.8, \ \rho = 2.0951 \text{ Å}.
$$

The quantum Sutton-Chen potential [51] is employed to model the gold substrates. This potential retains the simplicity of the original Sutton-Chen potential [52] given by

$$
V = \epsilon \sum_i \left[\sum_j v_2(r_{ij}) + c\sqrt{\varrho_i} \right]
\tag{2.8}
$$

where $v_2(r_{ij}) = \left(\frac{\rho}{r_{ij}}\right)^n$ is the pair potential that accounts for the repulsion between atoms i and j. $\varrho_i = \sum_j \left(\frac{\rho}{r_{ij}}\right)^m$ is a local density term accounting for the cohesion associated with atom i. ρ is the lattice parameter c is a dimensionless parameter. Quantum corrections to better predict mechanical properties involving defects, surfaces and interfaces yielded the following parametric set:

$$
\epsilon = 7.8052 \times 10^{-3} \text{ eV}, \ c = 53.581,
$$

$$
n = 11, \ m = 8, \ \rho = 4.0651 \text{ Å}.
\tag{2.9}
$$

CHAPTER 3   MOLECULAR DYNAMICS STUDIES OF PLASTIC DEFORMATION DURING SILICON NANOINDENTATION

Anil Gannepalli[‡§] and Surya K. Mallapragada[‡*]

3.1   Abstract

Molecular dynamics studies are performed to investigate the evolution of the deformed region during nanoindentation of silicon. A new approach based on a local strain diagnostic to identify and characterize the plastic rearrangements occurring during indentation is presented. During indentation, the response of the substrate changes from elastic to plastic to relieve the accumulated stress. The plastic rearrangements involve the displacement of atoms from the lattice sites to interstitial sites. The formation of interstitials results in the transformation of the deformed region to a denser amorphous phase. During retraction of the tip, the deformed region undergoes an incomplete elastic recovery signifying the plastic nature of rearrangements.

3.2   Introduction

Scanning tunneling microscope (STM), atomic force microscope (AFM) and related microscopes have been demonstrated as tools for fabricating nanoscale structures - a top-down approach to nanotechnology. However, this technology has severe limitations in terms of throughput and reproducibility dur-

---

[‡]Department of Chemical Engineering, Iowa State University, Ames, IA 50011
[§]Primary researcher and author
[*]Author for correspondence, suryakm@iastate.edu

ing fabrication. In order to overcome the present limitations in nanofabrication and the future problems with working nanomachines, it is imperative to understand the underlying atomistic phenomena associated with material modification at the nanoscale. Molecular dynamics (MD) simulations, by virtue of their high temporal and spatial resolution, offer an ideal approach to gain insights into atomic-scale processes and understand their mechanisms. A remarkable enhancement in computational capability and high performance computation techniques has enabled researchers to employ both classical molecular dynamics [53, 54, 55, 56, 57, 58] and *ab initio* quantum mechanical methods [59, 60] to investigate the nanoindentation process and gain significant insights into atomistic behavior.

In this study, we investigate the deformation of a silicon substrate during indentation by a rigid tip and present a new approach, based on a local strain diagnostic, to identify and characterize the plastic deformation occurring during indentation.

3.3 Methodology

In the simulation, only the microscopic contact region between the tip and the surface is considered and the effects due to and on farther regions of the substrate are neglected. The atomic configuration of the system studied is illustrated in Figure 3.1. The substrate is modeled as a finite slab (58 Å × 58 Å × 20 Å) with 3872 silicon atoms placed in a diamond lattice with a reconstructed (100) surface exposed. All the boundary atoms of the substrate are fully constrained with the exception of those on the surface exposed to the tip. The substrate is sufficiently large to eliminate the affects of the finite substrate size on the results and observations made in this study. The tip is modeled as an assemblage of atoms in a diamond cubic lattice with a lattice spacing of 5.43Å. The tip atoms are arranged as a pyramid with exposed (111) facets and a 10 Å × 10 Å (100) indenting face. The size of the simulated tip is about 100 times smaller than the finest tips used in experiments.

We have employed the widely used Stillinger-Weber (SW) potential [50] to simulate the behavior of the dynamic silicon substrate. This potential has two and three-atom contributions, which vanish at the cut-off radius without any discontinuities and distinctly favor the tetrahedral geometry. The focus of this study is to investigate the atomistic processes occurring in the substrate during indentation by an infinitely hard tip. Thus the tip is modeled as a rigid body and the interactions between the tip and
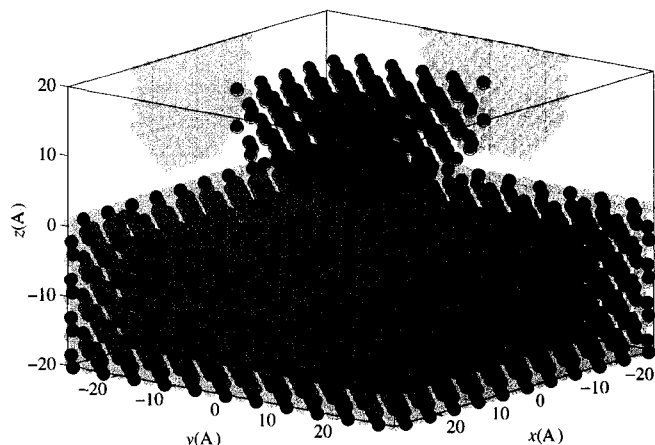
Figure 3.1   Initial configuration of the tip and the substrate. Red - tip atoms, dark
red - constrained boundary atoms, gold - dynamic substrate atoms.

substrate atoms are modeled by Lennard-Jones 12-6 potential for simplicity. The parameter values for

the potential (ϵ = 4.184 J, ρ = 2.095 Å) are chosen such that the physical interactions are adequately

modeled without any chemical effects.

We have used a modified version of a parallel molecular dynamics package DL_POLY [61] to per-

form the calculations. The motion of the atoms is evaluated by integrating the Newtonian equations

of motion using Verlet-Leapfrog method with a timestep of 0.1 fs. The tip is modeled as rigid by not

integrating the equations of motion of the tip atoms. The substrate is first equilibrated to its mini-

mum energy configuration at 300 K. The indentation is simulated by advancing the tip atoms at every

timestep giving the tip a velocity of 25 ms^{-1}. The temperature is regulated by periodically scaling the

velocities of the atoms of the two deepest non-constrained layers of the substrate, away from the con-

tact region to minimize the interference of the temperature control mechanism with the normal energy

flow processes that occur in the contact region.

It should be noted that the tip approach velocity of 25 ms is several orders of magnitude greater

than the dislocation velocity in silicon. Thus, the length and time scales of this study are too small to

study the propagation of the dislocations in the substrate. However, the results presented are legitimate

for a fast tip approach corresponding to high strain rates. In order to simulate a slow tip approach,

the substrate could be allowed to relax for an extended time after each translation of the tip into the

substrate [53, 62].

To understand the mechanics of plastic deformation during indentation we study the von Mises shear stress, $\sqrt{J_2}$, which is proportional to the square root of the distortion energy and is an indicator of the onset of plastic yielding [63] as proposed by von Mises. The von Mises shear stress is given by the square root of the second invariant of the deviatoric stress, J_2, which is defined as

$$J_2 = \frac{1}{2}\text{Tr}\left[(\boldsymbol{\sigma} - p\boldsymbol{I}) \cdot (\boldsymbol{\sigma} - p\boldsymbol{I})\right]. \tag{3.1}$$

where Tr denotes the trace of a matrix, $\boldsymbol{\sigma}$ is the atomic stress tensor [64], $\boldsymbol{I}$ is the unit matrix and p is the local hydrostatic pressure evaluated as one-third the trace of the atomic stress tensor.

Plastic deformation manifests itself as atomic rearrangements, and in order to identify and characterize these rearrangements we study a local strain diagnostic D^2_{min}, defined by Falk and Langer [65] as

$$D^2_{min}(\tau, t) = \sum_{N_c} \boldsymbol{R}_n \cdot \boldsymbol{R}_n, \tag{3.2a}$$

$$\boldsymbol{R}_n = (r_n(t) - r_0(t)) - \left(\boldsymbol{X}\boldsymbol{Y}^{-1}\right) \cdot (r_n(\tau) - r_0(\tau)), \tag{3.2b}$$

$$\boldsymbol{X} = \sum_{N_c} (r_n(t) - r_0(t))(r_n(\tau) - r_0(\tau)), \tag{3.2c}$$

$$\boldsymbol{X} = \Sigma_{N_c}(r_n(\tau) - r_0(\tau))(r_n(\tau) - r_0(\tau)). \tag{3.2d}$$

where the index n runs over the atoms in the neighborhood of the reference atom $(n = 0)$, $r_n(t)$ is position vector of nth atom at time t. The neighborhood is defined as the atoms within a distance of the SW cut-off radius and N_c is the coordination number defined as the number of atoms in the neighborhood at time t. Falk and Langer [65] studied the dynamics of viscoplastic deformation in a two-dimensional, two-component noncrystalline system and found to be an excellent diagnostic for identifying local irreversible transformations.

In this study we extend the use of D^2_{min} to identify structural transformations in a three-dimensional system. $D_{min}(\tau, t)$ is the local deviation from uniform strain during the time interval and it quantifies the atomic rearrangements in the neighborhood of an atom in that time interval. The cumulative strain, $D_{min}(\tau = 0, t)$, henceforth referred to as D_{min} for brevity, quantifies the local distortion in a region from its initial undisturbed state and is a good diagnostic for identifying deformed region. The incremental strain, $D_{min}(\tau = t - \Delta t, t)$, henceforth referred to as $\Delta D_{min}(\Delta t = 0.3\text{ps})$, is a measure of

the magnitude of local rearrangements that have occurred in the last $\Delta t(= 0.3\text{ps})$ time units. As plastic activity is associated with relatively large displacements of atoms, ΔD_{min} is indicative of plastic activity in the region.

3.4 Results and Discussion

The force versus displacement curve for the initial stages of indentation is shown in Figure 3.2. The force, F_z, is calculated as the sum total of the forces exerted on the tip atoms by the substrate and the displacement, z_{sep}, is the separation between the apex of the tip and the surface of the substrate before indentation. Initially, the indentation curve displays elastic behavior of the deformed region until the force on the tip decreases abruptly (at point d). This decrease in force is associated with a plastic deformation of the substrate to relieve the stress, in support of other theoretical investigations [53, 56].
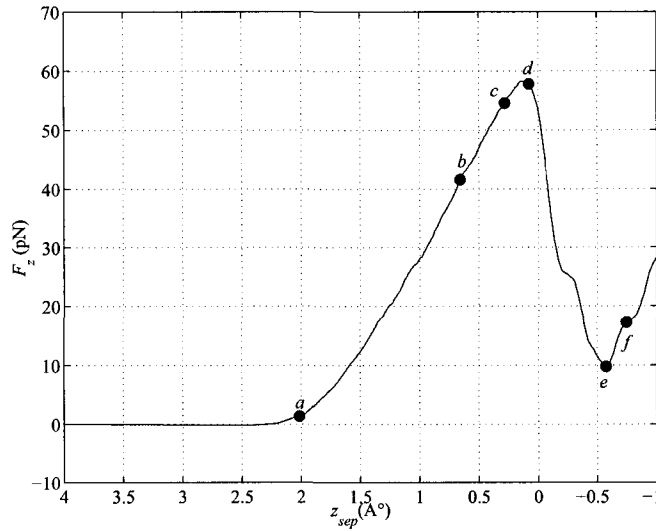
Figure 3.2 Force versus distance curve for Si(100) during the elastic response. (a) contact formation; (a) − (c) elastic response; (d) onset of plastic deformation; (e) completion of plastic deformation.

Further insight into this behavior is provided by the von Mises shear stress and strain profiles in the substrate. Figures 3.3, 3.4 and 3.5 show the von Mises shear stress ($\sqrt{J_2}$), cumulative strain (D_{min}) and incremental strain (ΔD_{min}) profiles in the region directly beneath the tip at various stages of indentation marked $a − f$ in Figure 3.2. Figures 3.3(a), 3.4(a) and 3.5(a) show that during contact
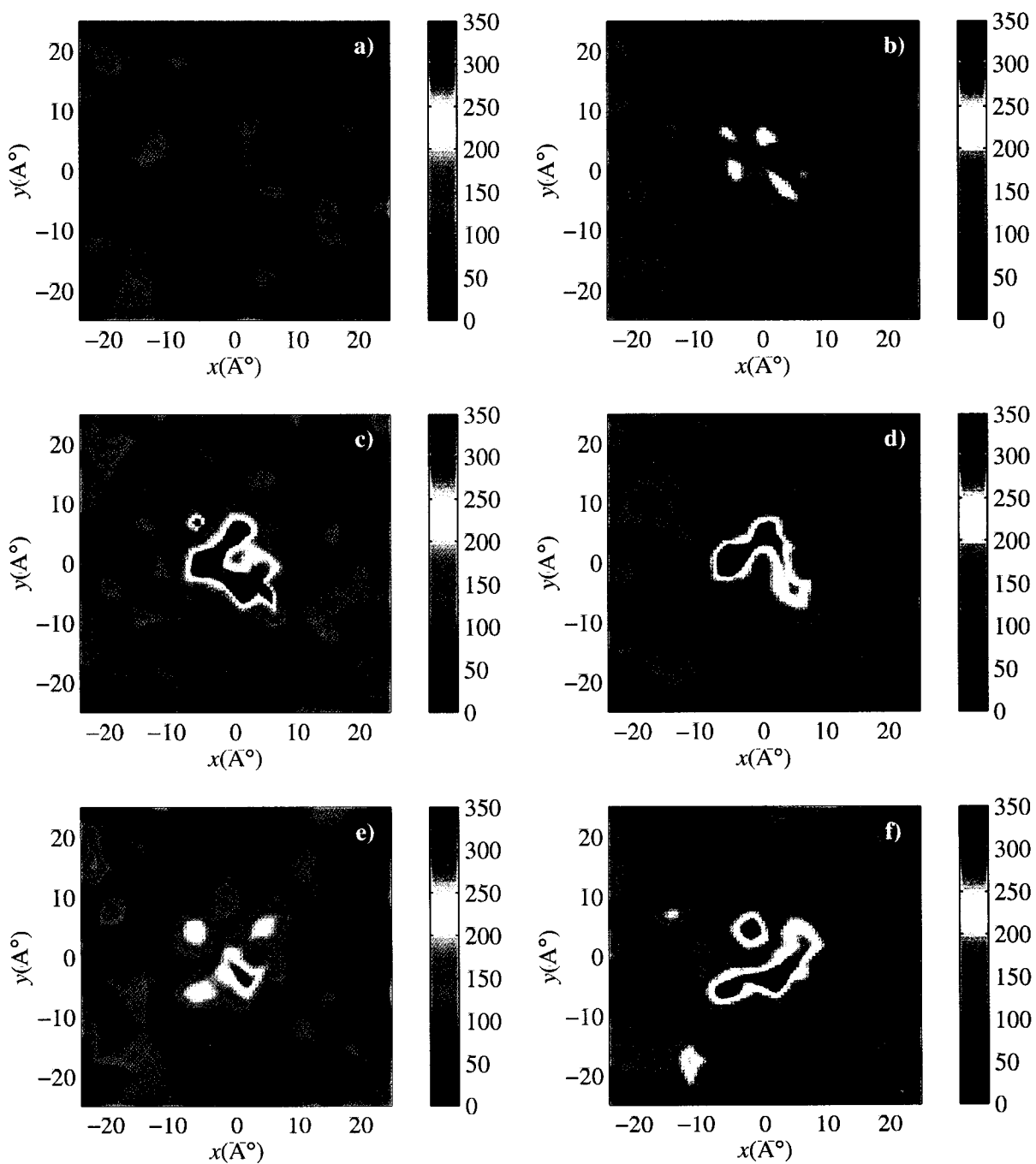
Figure 3.3   Calculated von Mises shear stress ($\sqrt{J_2}$, kbar) plots on a surface just
beneath the tip at indentation depths of: (a) 2 Å, (b) 0.7 Å, (c) 0.3 Å,
(d) 0.15 Å, (e) -0.5 Å, (f) -0.7 Å.

Figure 3.4   Calculated cumulative strain (D_{min}) plots on a surface just beneath the
tip at indentation depths of: (a) 2 Å, (b) 0.7 Å, (c) 0.3 Å, (d) 0.15 Å,
(e) -0.5 Å, (f) -0.7 Å.

Figure 3.5   Calculated incremental strain (ΔD_{min}) plots on a surface just beneath the tip at indentation depths of: (a) 2 Å, (b) 0.7 Å, (c) 0.3 Å, (d) 0.15 Å, (e) -0.5 Å, (f) -0.7 Å.
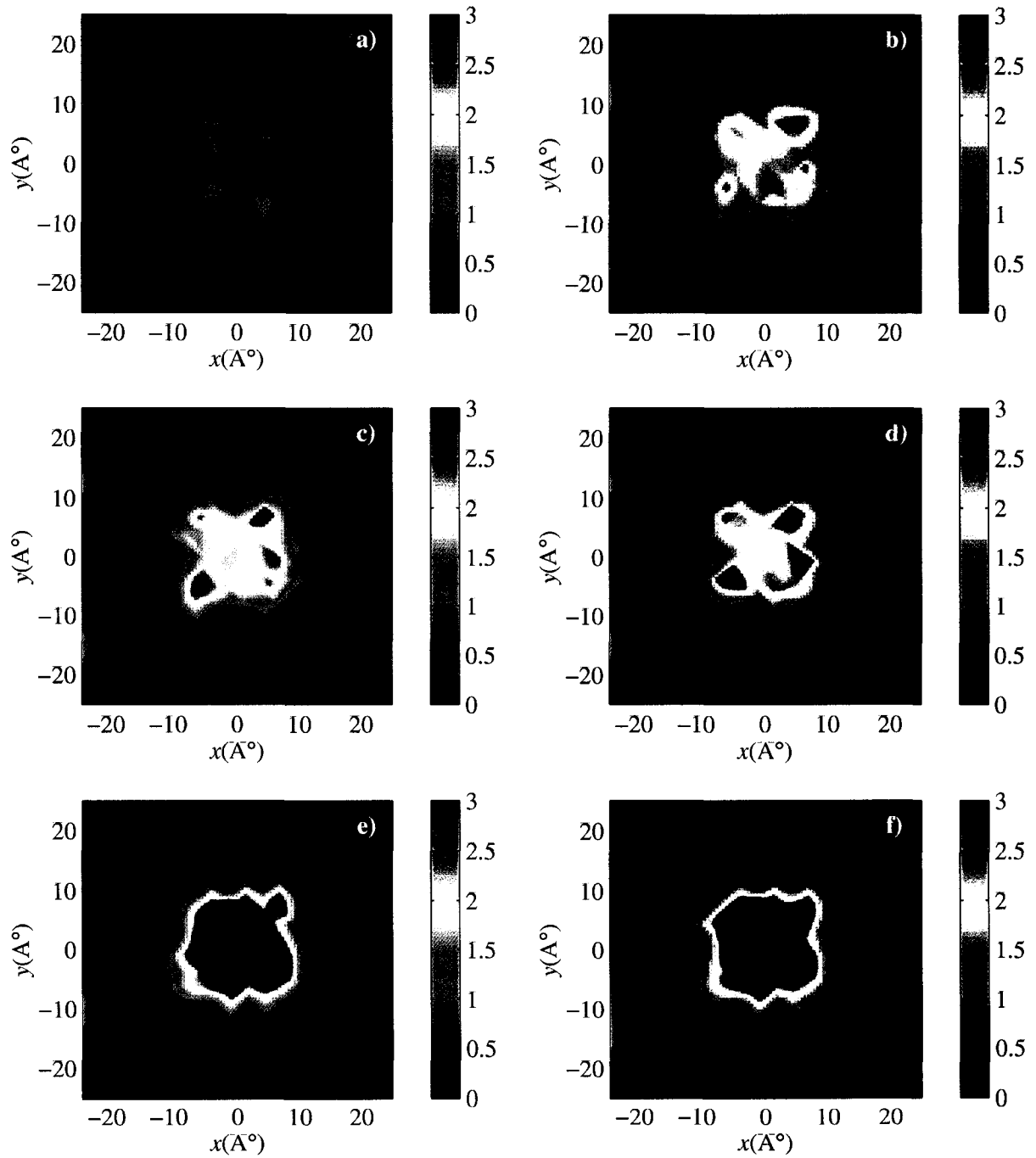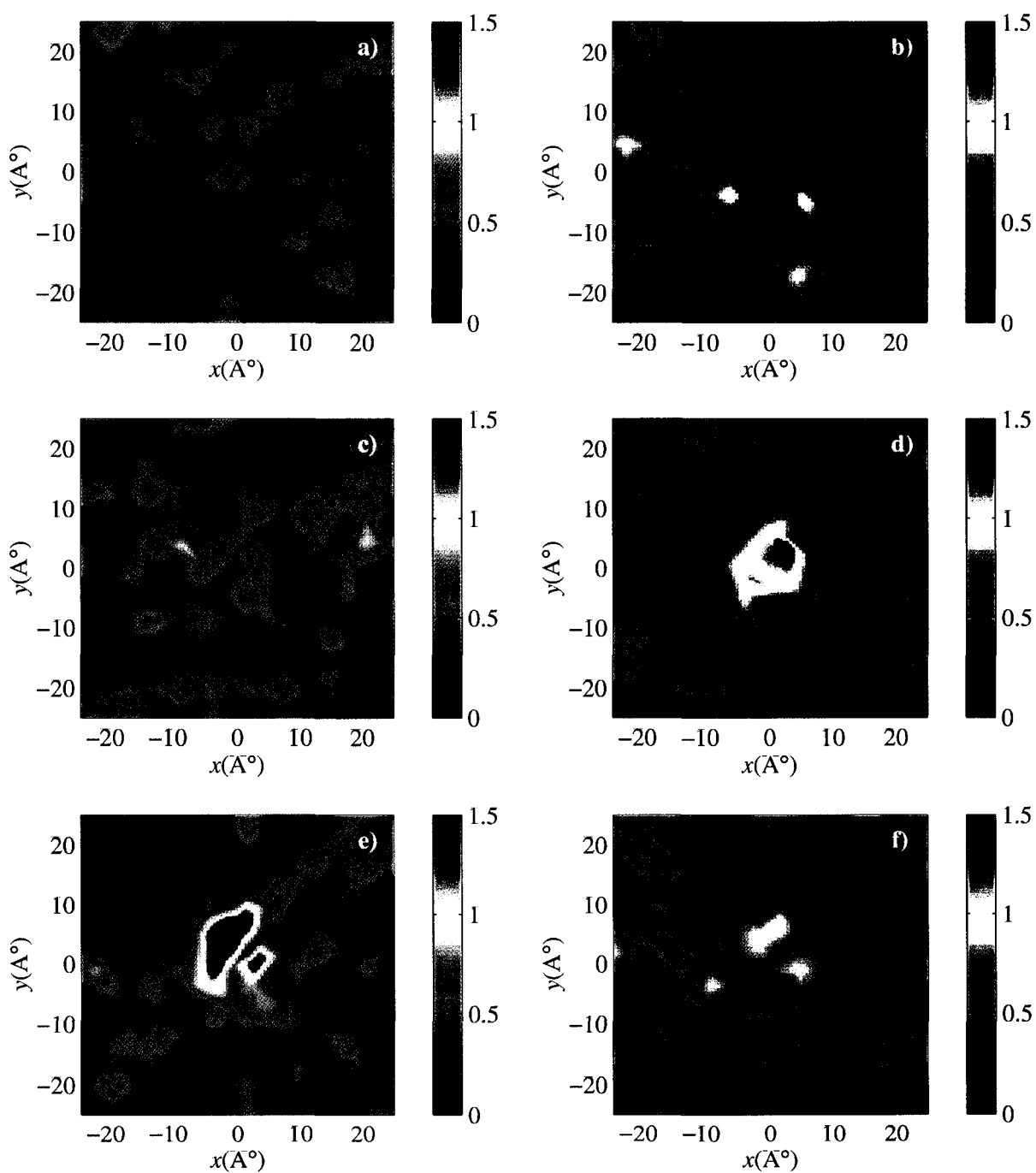
formation (point a), in the absence of large tip-substrate adhesive interactions, there is no significant stress in the contact region, very small deformation at the periphery of the contact and virtually no rearrangements. As the indentation proceeds from a to c the amount of deformation increases as seen in Figures 3.4(b), (c). From Figures 3.3(b), (c) and 3.5(b), (c), an increase in von Mises shear stress, a measure of the elastic stored energy, together with the small ΔD_{min} values suggest elastic response in this regime. Furthermore, it is seen that the peripheral atoms in the contact region are under higher stress in agreement with the findings of Landman *et al* [53].
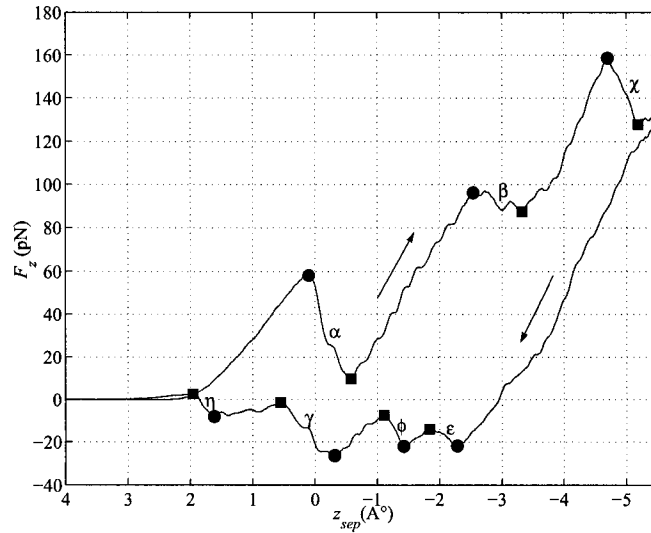
Figure 3.6   Force versus distance curve for Si(100) during the indentationretraction cycle. α, β, χ, ϵ, ϕ, γ and η represent the plastic rearrangements with solid circles corresponding to the onset and solid squares corresponding to the completion.

Upon further indentation, the shear stress increases, until it is relieved by a plastic deformation induced at point d in Figure 3.2. This process is illustrated in Figures 3.3(d) − (f), 3.4(d) − (f) and 3.5(d) − (f). At point d, we observe lower stresses, significant increase in deformation and large ΔD_{min} values, all indicative of plastic activity. This behavior of the material is in accordance with the von Mises criterion, which suggests a critical value for the von Mises shear stress for the onset of plastic deformation [63]. This plastic response continues through point e, where the stress has been completely relieved as exhibited in Figures 3.3(e), 3.4(e) and 3.5(e) and the response changes to elastic by point f as seen in Figures 3.3(f) and 3.5(f). From the above discussion it follows that during indentation a

maximum-minimum pair in the force curve represents a plastic event with the maximum corresponding to the onset and minimum to the completion of the process. From Figure 5(e) the critical maximum value of the von Mises stress is found to be about 300 kbar, which is about 4 times the uniaxial yield strength of 70 kbar. The large critical value can be attributed to the large strain rates, which have been found to increase the yield strength in silicon [66].
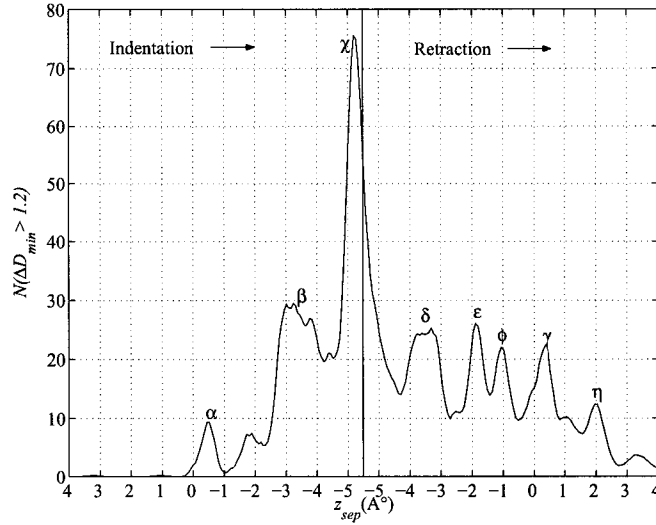
Figure 3.7   Variation in the number of rearrangements $(N(\Delta D_{min} > 1.2))$ with distance during indentation and retraction. The peaks at α, β, χ, δ, ϵ, ϕ, γ and η represent the plastic rearrangements.

Figure 3.6 shows the response of the silicon substrate to a full cycle of indentation and retraction. It is seen that further indentation beyond the first set of plastic rearrangements (α) results in more plastic events at β and χ. It is important to note that these deformations occur at higher forces suggesting an increase in the stress required to induce the plastic rearrangements as the deformation increases. This behavior is indicative of work hardening at the atomic level. On retracting the probe from the substrate, we see more activity at ϵ, ϕ, γ and η in the force-curve that is associated with plastic events, as observed by other researchers in metallic systems [53, 56].

To further investigate these rearrangements, we chose $D_{min} > 2.0$ to characterize the deformed region and $\Delta D_{min} > 1.2$ to characterize the rearrangements that make up a plastic event. Since the distribution of D_{min} and ΔD_{min} values is observed to be smooth, the choice of the cutoffs is somewhat arbitrarily based on the observation that D_{min} and ΔD_{min} values are less than their respective cutoffs

Figure 3.8   Variation in the (a) number of deformed atoms $(N(D_{min} > 2.0))$ and
(b) rate of change of the number $(\partial N(D_{min} > 2.0)/\partial t)$ with distance
during indentation and retraction. α, β, χ, δ, ϵ, ϕ, γ and η represent
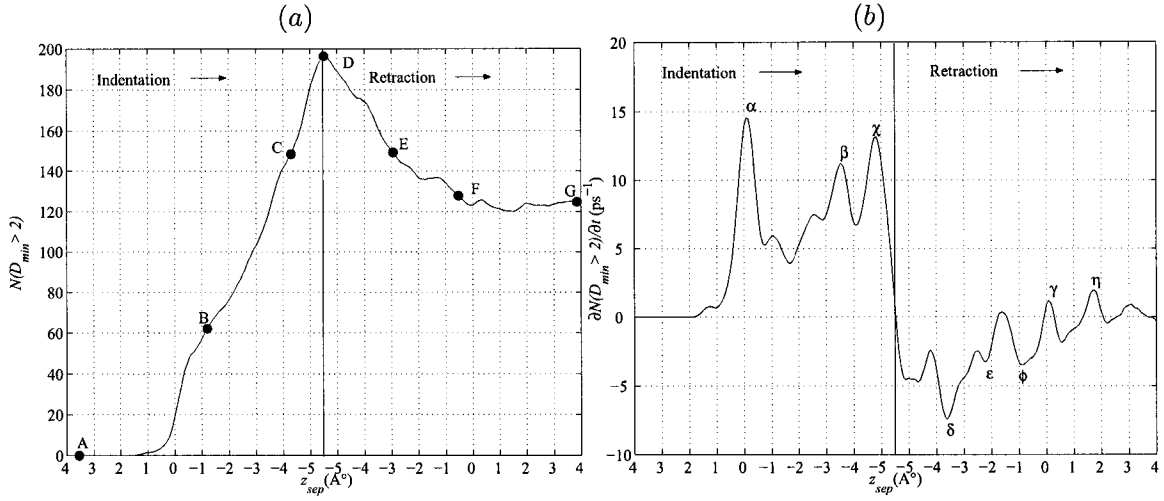the plastic rearrangements.

prior to the first plastic event (α). However, it is important to note that Figures 3.7 and 3.8 are quite insensitive to the choice of the cutoffs. These cutoffs can be expected to be different for different materials and in general depend on the physics of the computer experiment. There are no a priori criteria for the choice of the cutoffs and they have to be selected based on the observed distribution of the values. Therefore, D_{min} serves as an excellent qualitative diagnostic, rather than a quantitative measure, to identify atomic rearrangements. From above and earlier discussion it is reasonable to hypothesize that, in this simulation, plastic deformation is associated with an increase in the number of deformed atoms, $N(D_{min} > 2.0)$, during the event. Also, the number of atoms associated with rearrangements, $N(\Delta D_{min} > 1.2)$ would peak during the event. Figures 3.7, 3.8(a) and (b) show the variations in $N(\Delta D_{min} > 1.2)$, $N(D_{min} > 2.0)$ and $\partial N(D_{min} > 2.0)/\partial t$ during the indentation-retraction cycle. From Figures 3.6 and 3.7 it is seen that, except for the event δ, which is not discernible in the force-curve (Figure 3.6), the peaks are well correlated to the plastic events observed in the force-curve. The width of a peak signifies the duration of the event and the height is a measure of the magnitude of the event. It is interesting to note that in Figure 3.6, the maxima correspond to the onset and the minima to the completion of event during indentation. This observation is reversed during retraction.
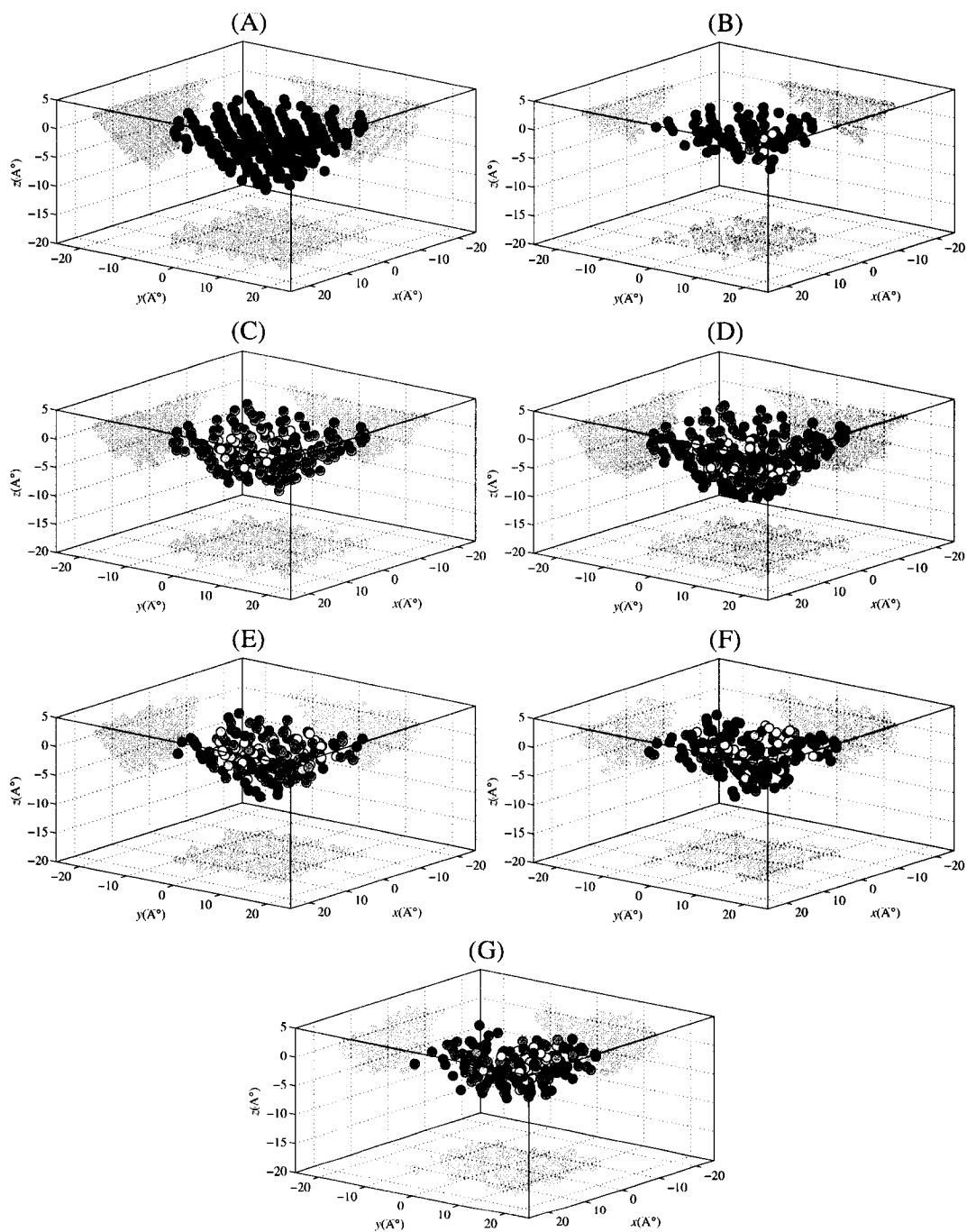
Figure 3.9 Snapshots of the deformed region at various stages of indentationre-traction cycle as marked in Figure 3.8(a). (A) 3.5 Å; (B) -1.2 Å; (C) -4.2 Å; (D) -5.5 Å; (E) -3 Å; (F) -0.5 Å; (G) 4 Å. Colorscale represents the extent of deformation with dark blue indicating D_{min} = 2.0 and red D_{min} = 5.0.

Figure 3.8(a) shows an increase in the number of deformed atoms during indentation, but a decrease during retraction, indicating an elastic recovery. This is corroborated by the observation that the rearrangements at δ, ϵ and ϕ in Figure 3.7 correspond to the minima in Figure 3.8(b). This recovery however is not complete, as the substrate has undergone some irreversible rearrangements that result in the hysteresis observed in the indentation-retraction cycle. It can be expected that the above results would be qualitatively similar for other empirical potentials used to simulate silicon.
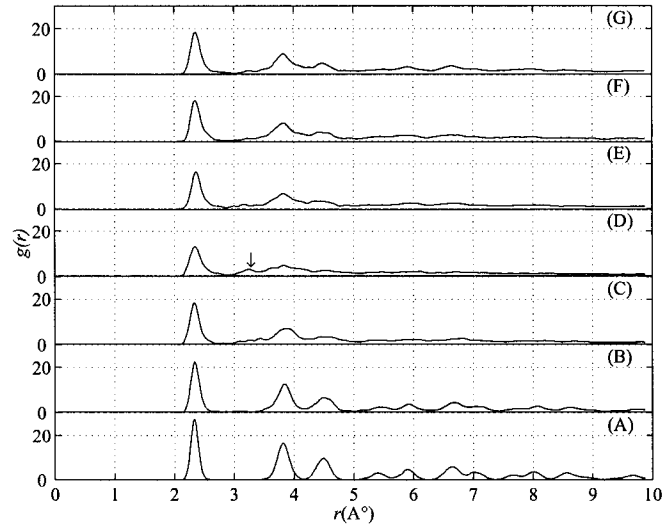
Figure 3.10   The radial distribution function for the deformed region at various
stages of indentationretraction cycle as marked in Figure 3.8(a). (A)
3.5 Å; (B) -1.2 Å; (C) -4.2 Å; (D) -5.5 Å; (E) -3 Å; (F) -0.5 Å; (G) 4
Å.

The plastic deformation processes are further illustrated in Figures 3.9 and 3.10 which depict the evolution of the deformed region through various stages of the indentation-retraction cycle marked A, B, C, D, E, F and G in Figure 3.8(a). During the indentation, the temperature in the deformed region varies within a range of 300K to 420K. It is seen from Figure 3.9(A) that the shape of the deformed region, in its undisturbed state, is similar to that of the tip, as noted by Brenner *et al* [55]. However, they claim that this similarity is lost during plastic deformation as opposed to the depictions in Figures 3.9(B)-(D). This incongruency in the observations could be due to either the different empirical potential employed or the different tip shapes used. To study the structural character of the deformed region in the substrate we evaluated the pair distribution functions as shown in Figure 3.10. It is seen

that prior to indentation, the distribution function in Figure 3.10(A) resembles closely to that of a crystalline structure with long-range periodicity indicative of an undisturbed crystalline structure. As the tip indents the substrate (B)-(D), the region slowly loses its long-range periodicity and at the maximum indentation depth, the distribution resembles to that of amorphous silicon as depicted in Figures 3.10(B)-(D). In Figure 3.10(D), the peak at 3.3Å, shown by the arrow, is usually observed in amorphous SW silicon [66]. The evolution of the amorphous phase is exemplified in Figures 3.9(B)-(D). During indentation, the tip is accommodated without any extrusion of the substrate atoms above the surface [55] by the plastic flow of the atoms to the interstitial sites [59]. This formation of interstitials disrupts the crystallinity and results in a densification transformation to amorphous phase, which can accommodate the tip without extrusion of substrate atoms. This process is further illustrated in Figure 3.11 as an increase in the mean coordination number (N_c) in the deformed region during indentation.
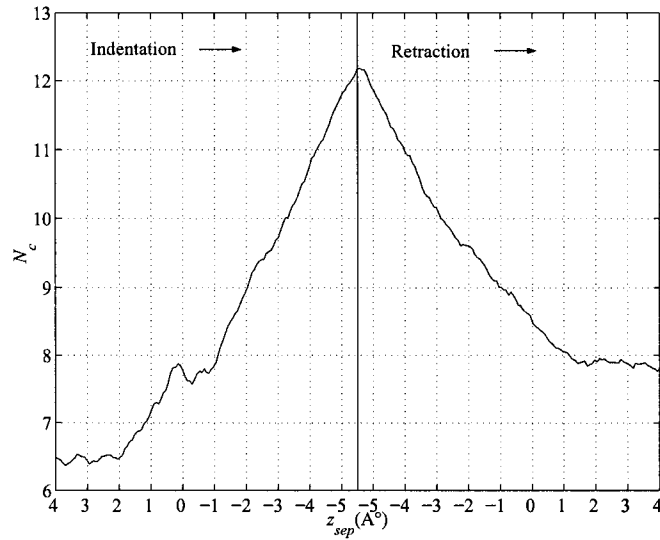
Figure 3.11   Variation in the coordination number (N_c) during the indentationretraction cycle.

During retraction, the process of elastic recovery is very lucidly seen in Figures 3.9(D) and (E) where the lower most atoms of the deformed region at maximum indentation (point D) have returned to their initial positions (point E). However, this recovery is not complete as seen in Figure 3.9(G). In Figures 3.10(D)-(G), the elastic recovery in the deformed region manifests as slow reclamation of its short-range periodicity to a certain extent but no long-range periodicity is observed upon complete

retraction, suggesting an incomplete elastic recovery as observed before.

Our observations of amorphous silicon in the deformed region corroborate the findings of Kallman *et al* [54]. High-resolution transmission electron microscopy (TEM) of the region beneath the indentor has showed [67, 68] the characteristic pattern of an amorphous material, in support of our finding. A few other experimental [69, 70, 71] and theoretical [58, 72] indentation studies have suggested the transformation to a β-Sn structure, which has been reported [73, 74] as one of the high-pressure phases of silicon occurring under high hydrostatic pressure conditions. Another investigation [75] suggests the phase transformation to BC8 or amorphous depending on the indenter size. Our failure to observe the phase transformations to β-Sn or BC8 structure could be attributed to the presence of high shear stresses, which have been found to induce amorphization in silicon [76]. Another possibility, which in our opinion is a more plausible explanation, is the inability of the SW potential to capture the transformation to a β-Sn structure under high hydrostatic pressures.

3.5 Concluding Remarks

The plastic deformation processes during nanoindentation of silicon through molecular dynamics simulations have been investigated. We have presented a new approach, based on a local strain diagnostic, to identify the plastic rearrangements and the extent of deformation during nanoindentation. During indentation, the substrate initially responds elastically resulting in a build up of von Mises shear stress. With the progress of indentation, the stress is relieved by plastic deformation, which involves the displacement of atoms from their lattice positions to the interstitial sites. Further indentation results in more plastic deformations at higher stresses, exhibiting strain hardening at the atomic scale. The formation of these interstitials during plastic deformation results in a densification transformation to amorphous phase in the deformed region that is able to accommodate the tip without any extrusion of substrate atoms above the surface. Upon retraction of the tip, the deformed region undergoes a partial elastic recovery indicating the irreversibility of the plastic rearrangements during deformation that manifests in the force-curve as a hysterisis.

CHAPTER 4   ATOMISTIC STUDIES OF DEFECT NUCLEATION DURING NANOINDENTATION OF Au(001)

Anil Gannepalli[‡§] and Surya K. Mallapragada[‡*]

4.1   Abstract

Atomistic studies are carried out to investigate the formation and evolution of defects during nanoindentation of a gold crystal. The results in this theoretical study complement the experimental investigations [J. D. Kiely and J. E. Houston, Phys. Rev. B **57**, 12588 (1998)] extremely well. The defects are produced by a three step mechanism involving nucleation, glide and reaction of Shockley partials on the {111} slip planes noncoplanar with the indented surface. We have observed that slip is in the directions along which the resolved shear stress has reached the critical value of approximately 2 GPa. The first yield occurs when the shear stresses reach this critical value on all the {111} planes involved in the formation of the defect. The phenomenon of strain hardening is observed due to the sessile stair-rods produced by the zipping of the partials. The dislocation locks produced during the second yield give rise to permanent deformation after retraction.

4.2 Introduction

Understanding the detailed mechanics of material deformation is a fundamental challenge in materials science. In metals, the defect structures produced during deformation influence the material properties and behavior critically [77, 78]. The formation and evolution of such structures have their basis in atomistic processes and the study of these nanoscale phenomena is paramount to the understanding of macroscopic phenomena such as fracture, friction, strain hardening and adhesion. The results of such research will also greatly facilitate the design of novel materials with desired properties. These insights into material behavior can be exploited to create desired dislocation patterns which can then be etched in a controlled manner to fabricate nanopatterns and nanostructures [79].

Nanoindentation experiments, with the advent of scanning probe microscopes and advances in indentation techniques, are capable of experimentally probing material properties and phenomena at the nanoscale [44, 45, 46]. At these atomic length scales, the continuum models of deformation do not perform well and atomistic methods need to be considered to investigate the nanoscale deformation behavior. Advances in computational capability and high performance techniques have enabled researchers to investigate nanoindentation studies of comparable length scales theoretically using molecular dynamics simulations [57, 80]. The experiments, for the most part, have emphasized quantitative investigation of mechanical properties by measuring the force displacement curves, and the theoretical computer simulations have been targeted at studying the atomistic processes involved in plastic deformation during indentation experiments. The primary goal of such studies is to complement the experimental findings with theoretical investigations in understanding the mechanisms of plastic deformation in materials.

In this paper, we present results of atomistic studies of nanoindentation of a passivated gold surface. The objective of this work is to study the atomistic processes responsible for plastic yield during the initial stages of indentation and explain the experimentally observed yield phenomena and defect structures [45].

4.3 Methodology

The objective of this atomistic study is to investigate the defect nucleation during nanoindentation of a passivated Au(001) surface and study the mechanisms leading to plastic deformation. The atomic

configuration of the system studied is illustrated in Figure 4.1. The gold substrate is modeled as a slab

(122 Å × 122 Å × 50 Å) containing 46400 atoms with periodic boundary conditions parallel to the

surface. The orientation of the slab is such that the directions [100], [010] and [001] coincide with x,

y and z. The bottom layer is fully constrained and the substrate size is sufficiently large to eliminate

the finite size effects. The indenter is an assemblage of atoms in diamondoid cubic lattice arranged as

a truncated pyramid with exposed (111) facets and a 15 Å × 15 Å (001) square indenting face. The

indenter is oriented such that the edges of the indenting face are in [1̄10] and [1̄1̄0] directions with

respect to the gold crystal.
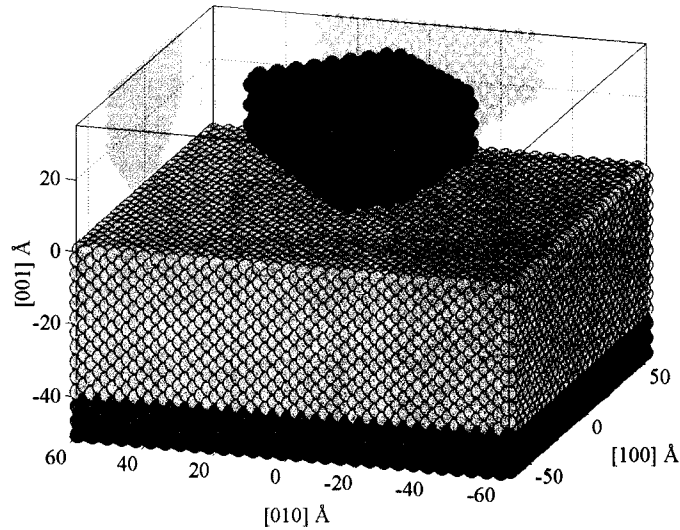
Figure 4.1   Atomic configuration of the indenter and the gold substrate. Red -
indenter; orange - dynamic gold substrate; gold - temperature control
region; dark red - fully constrained boundary. The indenting face is
a square with edges along the [1̄10] and [1̄1̄0] directions of the gold
crystal.

We have employed the quantum Sutton-Chen (Q-SC) [51] potential to model the gold atoms. This

formulation includes the quantum corrections to better predict mechanical properties, and retains the

simplicity of the original Sutton-Chen potential [52] to facilitate the understanding of the underlying

physics of various processes. The indenter is modeled as a rigid body and the indenter-surface interac-

tions are purely repulsive, $V(r) = \epsilon(r/\rho)^{-12}$ with $\epsilon = 25$ meV and $\rho = 3$ Å , to eliminate the adhesive

interactions and mimic the passivation of the gold surface in experiments.

We have used an extended version of the parallel MD package DL_POLY [61] to perform the calculations. The dynamics of the substrate is evaluated by integrating the Newtonian equations of motion using Verlet-leapfrog method with a timestep of 1 fs. The gold substrate is equilibrated to its minimum energy configuration at 300 K and the indentation is simulated by advancing the indenter atoms by 0.0005 Å at every timestep, giving the indenter a velocity of 50 m/s. The temperature is regulated by periodically scaling the velocities of the atoms of the deepest non-constrained region of the substrate, away from the contact region to minimize the interference of the temperature control mechanism with the normal energy flow processes that occur in the contact region.

To understand the mechanics of plastic deformation during indentation, atomic stress tensor [64] σ is used to study the distribution of stresses. The von Mises shear stress, $\sqrt{J_2}$, proportional to the square root of the distortion energy, is an indicator of the onset of plastic yielding [63] as proposed by von Mises. The von Mises shear stress is given by the square root of the second invariant of the deviatoric stress, J_2, which is defined as

$$J_2 = \tfrac{1}{2}\mathrm{Tr}\left[(\sigma - p\boldsymbol{I}) \cdot (\sigma - p\boldsymbol{I})^{\mathrm{T}}\right], \tag{4.1}$$

$$p = -\tfrac{1}{3}\mathrm{Tr}(\sigma). \tag{4.2}$$

where Tr denotes the trace of a matrix, $\boldsymbol{I}$ is the unit matrix and p is the local hydrostatic pressure.

In metals, plastic deformation occurs by the glide of dislocations on the slip planes. In order to identify and characterize the dislocations being nucleated during indentation we employ the slip vector analysis,[80] which provides information on the Burgers vectors of dislocations. The slip vector is defined as,

$$s = \frac{1}{n_s}\sum_{\beta}^{n_s}\left(r_t^\beta - r_\theta^\beta\right). \tag{4.3}$$

where, n_s is the number of slipped neighbors β, of the reference atom, and r_t^β and r_θ^β are the vector differences of atom β and the reference atom positions at times t and θ, respectively. The slip vector given by the above expression represents the Burgers vector of slip between the plane containing atom α and its adjacent atomic planes, in the time interval $[\theta, t]$. However, this is true only in the case of single slip, where the reference atom is contained by only one slip plane. In the event of multiple slip, where the atom is contained by two planes undergoing slip simultaneously, the Burgers vector is

different from the slip vector given above. In any event, the slip vector will have a large magnitude for inhomogeneous, non-affine deformation near the atom and can be used to identify slipped regions.

The strains induced by indentation are studied by evaluating the atomic strain tensor as formulated by Horstemeyer and Baskes [81]. This formulation is based on the deformation gradient for a material employing many-bodied potential. The atomic Lagrangian Green strain tensor E, used in this study is given by,

$$E = \frac{1}{2}\left(F^{\mathrm{T}}F - I\right), \tag{4.4a}$$

$$F = XY^{-1}, \tag{4.4b}$$

$$X = \sum_{\beta}^{m}\left(r_t^{\beta} \otimes r_{\theta}^{\beta}\right), \tag{4.4c}$$

$$Y = \sum_{\beta}^{m}\left(r_{\theta}^{\beta} \otimes r_{\theta}^{\beta}\right). \tag{4.4d}$$

where, F is the deformation gradient, m is the number of nearest neighbors β of the reference atom, $r_{\theta}^{\beta}, r_t^{\beta}$ have the same meaning as above and $\otimes$ represents tensorial product. E will then quantify the strain experienced by the reference atom in the time interval $[\theta, t]$.

To investigate the mechanisms of dislocation nucleation and glide on the slip planes, we study the resolved shear stresses on the slip planes along the Burgers vectors given by the slip vector analysis. The resolved shear stress τ on a plane with normal $\hat{n}$ along the direction of slip $\hat{b}$ is given by,

$$\tau_{(n)[b]} = \hat{b} \cdot \sigma \cdot \hat{n} \tag{4.5}$$

Schmid law [82] states that a slip system is activated when the resolved shear stress on that system reaches a critical value called the critical resolved shear stress (CRSS).

4.4 Results and Discussion

4.4.1 Indentation

The force versus displacement curve for the initial stages of indentation is shown in Figure 4.2. The force F_z is calculated as the sum total of the forces exerted on the indenter atoms by the substrate and the displacement z_{sep} is the separation between the indenter apex and the surface of the substrate before

indentation. Initially, the force curve displays elastic behavior until the force decreases abruptly at the first yield point, marked as (1) in Figure 4.2. This phenomenon is associated with the nucleation of a plastic event to partially relieve the elastic stress in the contact region. This observation is in excellent agreement with other theoretical [53, 56, 83, 57, 80] and experimental results [45, 46, 44]. Upon further indentation the force begins to rise again, displaying yet another region of elastic behavior, until the substrate undergoes a second yield event (2) in Figure 4.2. It is interesting to see that the force curve has a higher slope in the second elastic response region and the second yield occurs at a higher force. This is indicative of strain hardening like behavior at the atomic scale resulting in an increase in the yield modulus and strength.
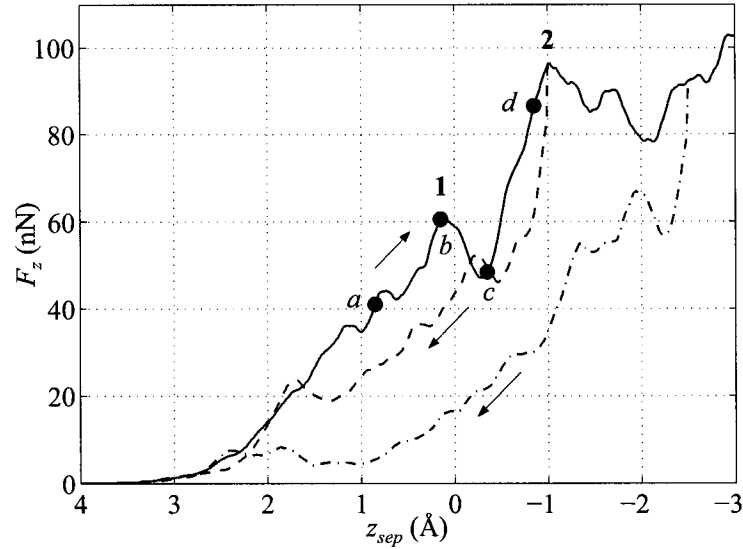
Figure 4.2   Force versus distance curve during initial stages of indentation. $(a) - (b)$ elastic response; (b) onset of first yield; $(b) - (c)$ first plastic yield event; $(c) - (d)$ second elastic response at a higher force and with a higher slope indicating strain hardening like behavior. 1 and 2 represent the first and second yield events.

4.4.1.1   First Yield : Defect Nucleation

To gain insight into this behavior, the evolution of the stress profiles in the contact region during indentation are analyzed. Figures 4.3 and 4.4 show the von Mises shear stress $\sqrt{J_2}$ and hydrostatic pressure p profiles in the region directly beneath the indenter at various stages of indentation marked
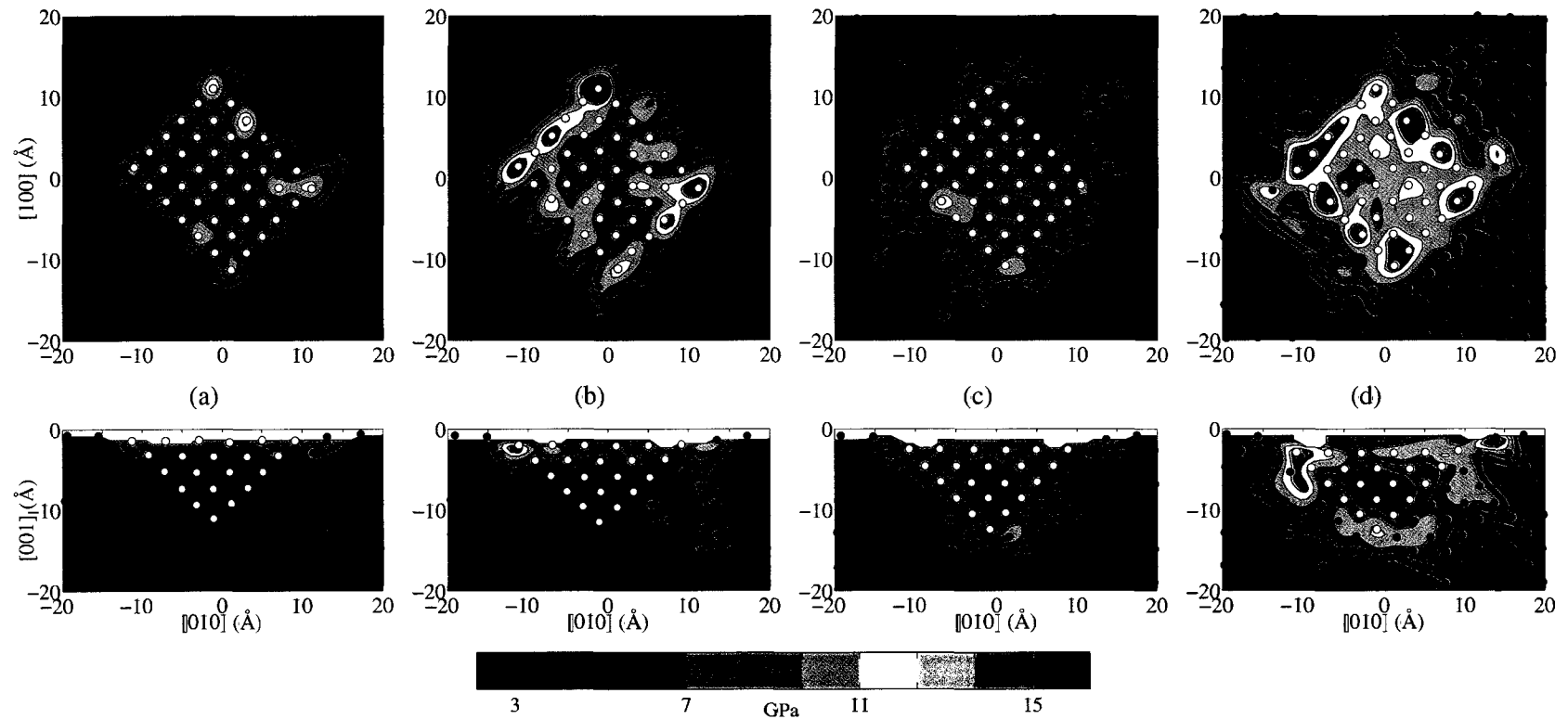
Figure 4.3 Contour plots of the atomic von Mises shear stress $\sqrt{J_2}$ in the indented
region at four stages of indentation marked $(a) - (d)$ in Figure 4.2. The
contours are on $[001]$ surface (upper row) just beneath the indenter
and $[100]$ surface (lower row) at $x = 0$. $\circ$ are the slipped atoms that
comprise the defect nucleated during the first yield event and $\bullet$ are the
undeformed atoms. Stress is concentrated at the corners of the contact
region. Increase in $\sqrt{J_2}$ from (a) to (b) and (c) to (d) signifies elastic
responses and a drop from (b) to (c) indicates plastic yield.
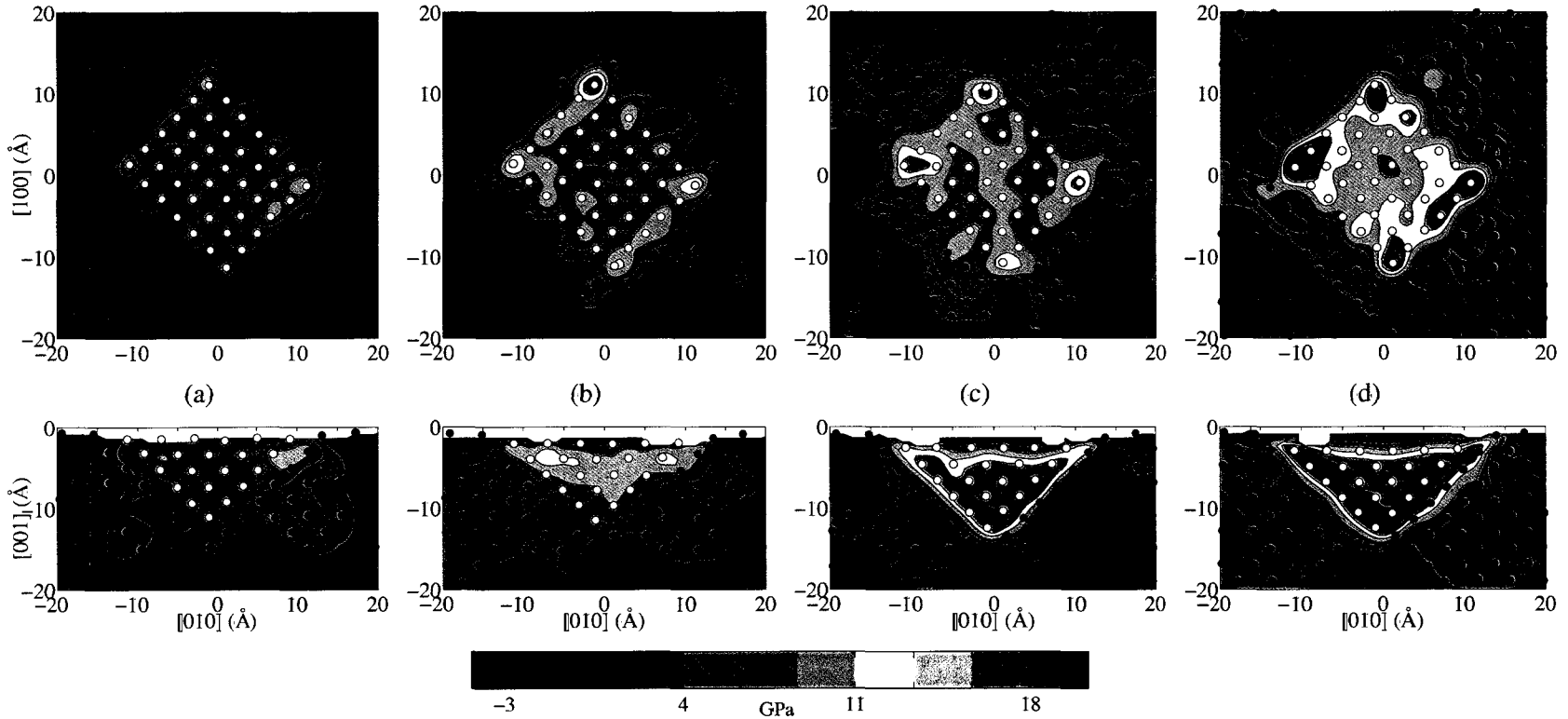
Figure 4.4 Contour plots of the atomic hydrostatic pressure p in the indented region at four stages of indentation marked $(a) - (d)$ in Figure 4.2. The contours are on [001] surface (upper row) just beneath the indenter and [100] surface (lower row) at $x = 0$. ○ are the slipped atoms that comprise the defect nucleated during the first yield event and ● are the undeformed atoms. Stress is concentrated at the corners of the contact region. After the first yield (c), a compressive strain of 0.052 in the defect gives rise to increased pressure of the order of $10 - 15$ GPa.

$(a) - (d)$ in Figure 4.2. Figures 4.3(a), (b) and 4.4(a), (b) show that as the indentation proceeds from (a) to (b), an increase in $\sqrt{J_2}$, a measure of the elastic stored energy, substantiates the elastic response seen in the force curve in this regime. At point (b) the elastic stress reach a threshold beyond which plastic deformation occurs that partially relieves and dissipates the elastic energy from the surface as seen in 4.3(c). This behavior is in accordance with the von Mises criterion,[63] which suggests a critical value for $\sqrt{J_2}$ for the onset of plastic activity. Upon further indentation from (c) to (d) $\sqrt{J_2}$ increases again implying another elastic response regime, which culminates in the second yield event.

To study the nature of plastic deformation and characterize the defect structures nucleated, the deformed regions are identified by the slip vector s_{01}, where 0 represents the initial undeformed state and 1 represents the state after the first yield event. Three snapshots of the deformed region at various stages of defect nucleation between (b) and (c) are shown in Figure 4.5 to illustrate the evolution of the defect structure. From the slipped atoms shown in Figure 4.5 it is seen that dislocation loops nucleate on the four $\{111\}$ planes at the surface and extend into the solid. These dislocation loops grow in size and intersect with the loops on the adjacent planes forming a pyramidal defect structure as seen in Figure 4.5(c). Figure 4.6 shows the corresponding slip vectors of the atoms on one of the slip planes, (111). From Figure 4.6(c) the magnitude of the slip vector of the atoms on the (111) plane is close to 1.66 Å along $[11\bar{2}]$, which is consistent with the $\langle 112 \rangle$ partial dislocations on $\{111\}$ planes in gold. The dislocation nucleated on the (111) plane is therefore the $\frac{1}{6}[11\bar{2}]$ Shockley partial, and similarly $\frac{1}{6}[\bar{1}1\bar{2}]$, $\frac{1}{6}[1\bar{1}\bar{2}]$ and $\frac{1}{6}[\bar{1}\bar{1}\bar{2}]$, partials are nucleated on $(\bar{1}11)$, $(1\bar{1}1)$ and $(\bar{1}\bar{1}1)$ planes, respectively. Thus the defect consists of intersecting intrinsic stacking faults on the four $\{111\}$ planes, which intersect the (001) surface with four fold symmetry. This pyramidal defect structure is in excellent agreement with the experimentally observed permanent deformation structures [45].

From continuum elastic theory [84] of indentation by a rigid flat frictionless punch, similar to the atomic indenter used in this study, the stresses reach a theoretically infinite value at the edges of the indenter. This observation, at the atomic scale, is validated by the large concentrations of stresses at the periphery of the contact region as seen in Figs. 4.3(b) and 4.4(b), in agreement with previous studies [53, 83]. Surface nucleation of partial dislocations in areas of enhanced stress is well supported experimentally [85, 86] and theoretical models of surface dislocation nucleation at

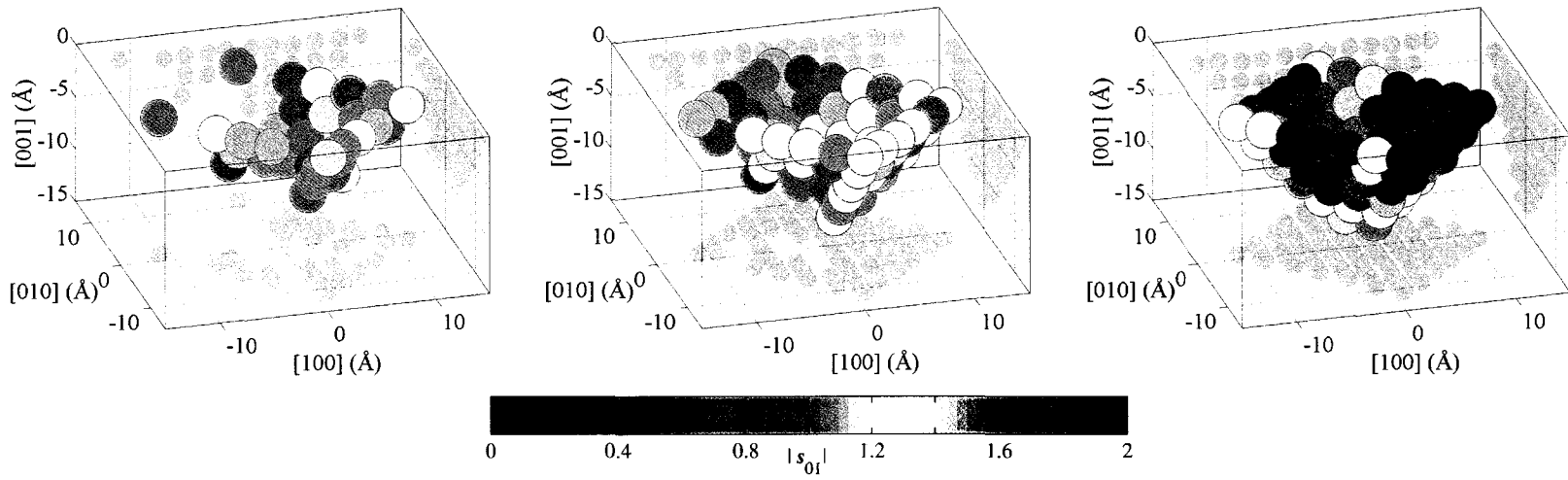Figure 4.5   Snapshots of deformed region depicting the evolution of the disloca-
tion structures nucleated during the first yield event $((b) - (c)$ in Fig-
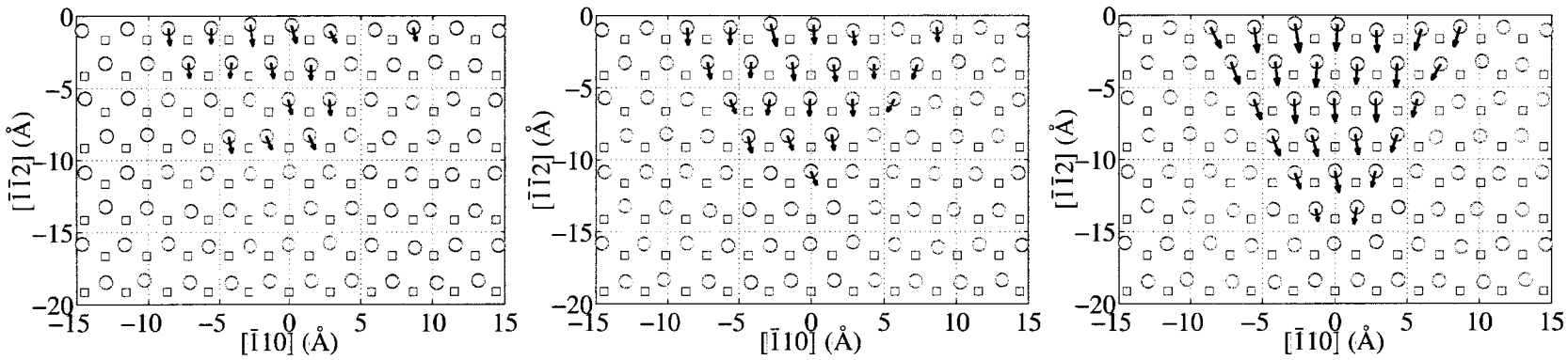ure 4.2). Colorscale represents $|s_{0\bar{1}}|$.

Figure 4.6 Slip vector (s_{01}) maps on (111) plane corresponding to the snapshots in Figure 4.5. ○ represent the atoms of the slipped plane and □ represent the atoms of the unslipped plane adjacent to the slipped region.

stress concentrators [87, 88, 89, 90] are well established. The corners of the contact region act as stress concentrators and serve as the sources for nucleation of Shockley partials on the surface. Under the influence of the stresses, these partials glide on the {111} planes, the dominant slip planes in gold, forming intrinsic stacking faults as seen in Figure 4.6. This slip results in the flow of part of the elastic energy from the contact surface to the sheared surfaces and is seen as an increase in $\sqrt{J_2}$ in the region of slip in Figure 4.3(c). The strain undergone by the atoms in the deformed region during defect nucleation is quantified by the mean Lagrangian strain tensor in Voigt notation, $\boldsymbol{E} = \begin{bmatrix} 0.068 & 0.064 & -0.166 & 0.007 & -0.002 & 0.02 \end{bmatrix}$. Thus the observed strain is in $\langle 100 \rangle$ directions and gives a volumetric strain of -0.052 in the pyramidal defect, giving rise to higher pressures of the order of $10 - 15$ GPa (with a bulk modulus of 207 GPa) above the ambient pressures as seen in Figure 4.4(c).
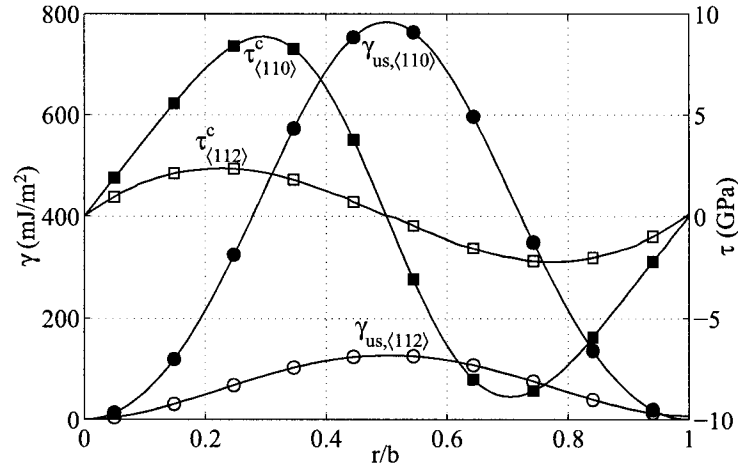
Figure 4.7   Generalized stacking fault energies γ (circles) and theoretical shear stresses τ^{th} (squares) for slip systems {111}$\langle 112 \rangle$ (open) and {111}$\langle 110 \rangle$ (solid). The slip vectors for the slip systems are $b_{\langle 112 \rangle} = \frac{1}{6}\langle 112 \rangle$ and $b_{\langle 110 \rangle} = \frac{1}{2}\langle 110 \rangle$. Lower $\tau^c_{\langle 112 \rangle}$ indicates a more energetically favorable {111}$\langle 112 \rangle$ slip system.

In order to understand why this particular slip system {111}$\langle 11\bar{2} \rangle$ has been activated, we study the resolved shear stresses (RSS), as the direction of slip has been associated with maximum RSS. Figure 4.8 shows the distribution of $\tau_{(111)[10\bar{1}]}$, $\tau_{(111)[01\bar{1}]}$ and $\tau_{(111)[11\bar{2}]}$ on the (111) slip plane along $[10\bar{1}]$, $[01\bar{1}]$ and $[11\bar{2}]$, respectively. These are the favored slip directions [91] on (111) plane for

the current stress state ($\sigma \approx \sigma_{zz}$). It is seen that even though $\tau_{(111)[10\bar{1}]}$ and $\tau_{(111)[01\bar{1}]}$ have higher concentrations near the surface than $\tau_{(111)[11\bar{2}]}$, the slip occurs along $[11\bar{2}]$. This incongruency of slip occurring in a lower RSS direction is consistent with the findings of other researchers [80] and can be explained by the concept of generalized stacking fault energy (GSF) γ, introduced by Vitek [92, 93]. GSF is the energy per unit area of a fault plane created by the rigid slip of one half of a perfect lattice relative to the other along a slip plane in a general slip direction. Figure 4.7 shows the unrelaxed GSF in the dominant slip directions [110] and [112]. It should be noted that unrelaxed GSF is a hypothetical concept that nevertheless offers valuable insight into the dynamics of slip.

The maximum value of γ in the direction of slip, called the unstable stacking energy γ_{us},[94] is the energy barrier to be overcome during slip. It is seen from Figure 4.7 that γ_{us} displays a strong directional dependence and slip along [112] has a much lower energy barrier than [110] and is thus more favorable as observed in this study. However, γ is a static quantity and is not an appropriate measure to describe the dynamics of slip. A better quantity would be the theoretical shear stress required to initiate and maintain the slip along the slip direction. This shear stress is given by

$$\tau_{\{n\}\langle r\rangle}^{th} = \frac{\partial \gamma_n}{\partial r} \tag{4.6}$$

where, γ_n is the GSF on a slip plane with normal n and r is the displacement vector. At any instant the atoms on a slip plane n slip along r if $\tau_{(n)[r]}$ exceeds $\tau_{\{n\}\langle r\rangle}^{th}$ and this instantaneous slip direction evolves continuously, resulting in relaxations as the slip proceeds. Among all the competing slip directions at every instant throughout the slip, such a mechanism results in the motion of atoms along a direction that has the smallest τ^{th}. Therefore, as the slip proceeds it traces a minimum energy path along a valley of the unrelaxed GSF energy landscape. The relaxed GSF energies are thus given by the valleys of the unrelaxed GSF energy landscape.

From the above discussion it follows that slip along a particular direction proceeds to completion if the resolved shear stress exceeds the maximum value of τth. This is the critical resolved shear stress (CRSS) τ^c referred to in Schmid law [82] as stated above. A plot of τth for slip on $\{111\}$ plane along $\langle 110 \rangle$ and $\langle 112 \rangle$ directions is shown in Figure 4.7. From Figs. 4.7 and 4.8 $\tau_{\{111\}\langle 112\rangle}^c$ is 2.34 GPa and is smaller than the observed $\tau_{(111)[11\bar{2}]}$ values. On the other hand $\tau_{\{111\}\langle 110\rangle}^c$ has a value of 8.88 GPa and is much higher than the observed $\tau_{(111)[10\bar{1}]}$ and $\tau_{(111)[01\bar{1}]}$ values. Thus, the observed slip direction

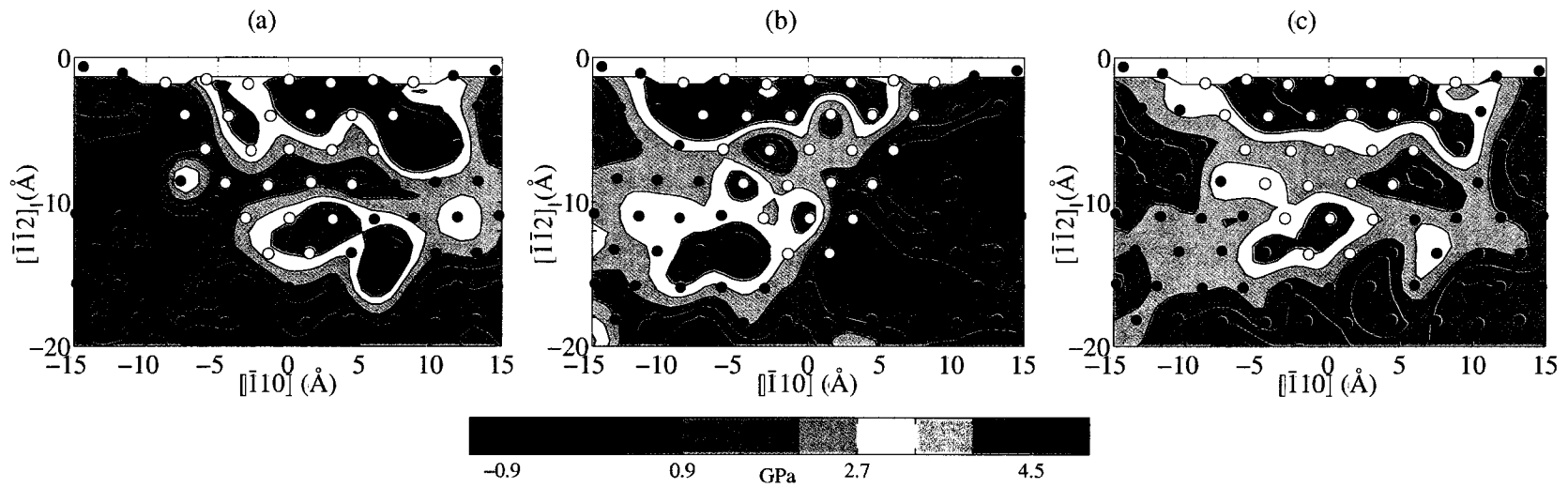Figure 4.8 Resolved shear stresses on (111) plane, just before the first yield point, along favored directions of slip: (a) $[01\bar{1}]$; (b) $[10\bar{1}]$; (c) $[11\bar{2}]$. ○ are the slipped atoms that constitute the stacking fault and ● are the atoms in the undeformed region. In some regions $\tau_{(111)\|11\bar{2}}$ is smaller than $\tau_{(111)\|10\bar{1}}$ and $\tau_{(111)\|01\bar{1}}$.

is $[11\bar{2}]$ rather than $[01\bar{1}]$ or $[10\bar{1}]$. Second and higher derivatives of γ could be used to further refine the dynamics of slip, but it is beyond the scope of this paper and for the present study τ would suffice.

The smallest of the directionally dependent τ^c representing the ideal shear strength of the crystal is 2.34 GPa in excellent agreement with the experimental estimates of 1.5 to 2.0 GPa [45, 44]. In Figure 4.8 the high τ values of 5 GPa greater than the theoretical estimate of the ideal shear strength might seem out of order, but it needs to be clarified that the theoretical value is based on a block like shear and such instantaneous rigid slip cannot be expected during the actual nucleation and propagation of slip. These τ values are also quite high compared to the experimental CRSS because the values in Figure 4.8 are highly localized and are inaccessible to experimental investigations. The shear stress values deduced from experiments represent the mean value of the shear stresses in the region local to indentation and a plot of such a mean of τ is shown in Figure 4.9. It can be seen that these values reach a maximum and drop abruptly at the first yield point validating the manifestation of Schmid law at the atomic scale. The maximum RSS on (111) is along $[11\bar{2}]$ and reaches a value of 1.95 GPa and on the other {111} planes the maximum RSS are in the range of 1.8 to 2.3 GPa. These values agree exceptionally well with the experimental estimates of 2 GPa.
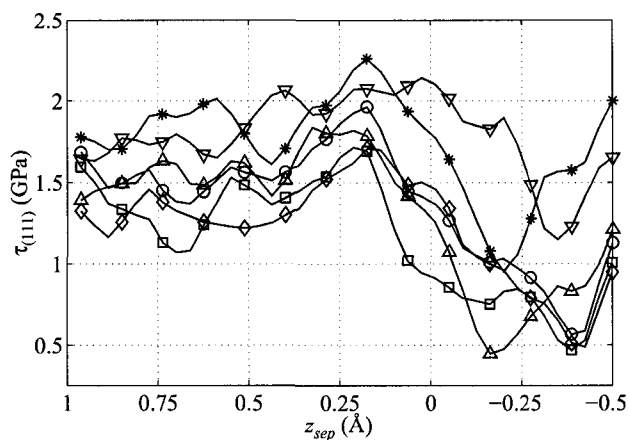
Figure 4.9   Mean resolved shear stresses in the deformed region for slip systems: □ $(111)[01\bar{1}]$; ◇ $(111)[10\bar{1}]$; ○ $(111)[11\bar{2}]$; * $(\bar{1}11)[\bar{1}1\bar{2}]$; ▽ $(1\bar{1}1)[11\bar{2}]$; △ $(\bar{1}11)[\bar{1}1\bar{2}]$. The resolved shear stresses reach a threshold at the yield point. The maximum resolved shear stress is in the range of $1.8 - 2.3$ GPa.

It is interesting to note that Schmid law and von Mises criterion, which have their origin in con-

tinuum mechanics, are also observed at the atomic scale. However, the yield mechanisms behind this phenomenological similarity are different resulting in very different magnitudes of critical stresses. In macroscopic yield the critical stresses are required to cause the motion of preexisting dislocations and/or multiplication of dislocations. Where as for yield at the defect free nanoscale, as is the case in this study, the critical stresses are required to nucleate dislocations at the surface.

The plastic strains produced by indentation are complex and activation of multiple slip systems is necessary to accommodate these general yields [95]. Groves and Kelly [96] have predicted the active slip systems by calculating the strain produced by a given slip system [97] and identifying the systems that contribute to the observed strain. Such a geometrical analysis [98] for compression in [001], which is the observed stress state just before the first yield point, predicts activation of slip on the four {111} planes resulting in plastic strains in $\langle 100 \rangle$. These predicted slip planes and strains are identical to those observed at the atomic scale in this study.

In the event of the presence of multiple sets of independent slip systems capable of producing the required strain, as is the case with f.c.c. crystals, Bishop and Hill [99, 100] proposed a stress criterion for yielding that requires the attainment of CRSS on the active slip systems, without exceeding CRSS on the inactive systems. The observed slip directions conform to the above criterion with the shear stresses reaching their critical values in $\langle 112 \rangle$, but not in $\langle 110 \rangle$.

4.4.1.2   Defect Nucleation Mechanism

Based on the results and discussion presented above, we propose a three step mechanism for the formation of the pyramidal defect during indentation of Au (001). It is convenient for the following discussion to use Thompson's notation for Burgers vectors and planes and refer to Figure 4.10 for an illustration of the mechanism.

Dislocation nucleation: Surface indentation of Au (001) with an indenter results in large concentration of stresses at the corners of the contact region. These stress concentrators, where the RSS on the {111} planes reach the CRSS, act as the sources for surface nucleation of Shockley partials ($\frac{1}{6}\langle 11\bar{2} \rangle$) B$\alpha$, A$\beta$, γD and δC on the slip planes ($\bar{a}$), ($\bar{b}$), (c) and (d) respectively.
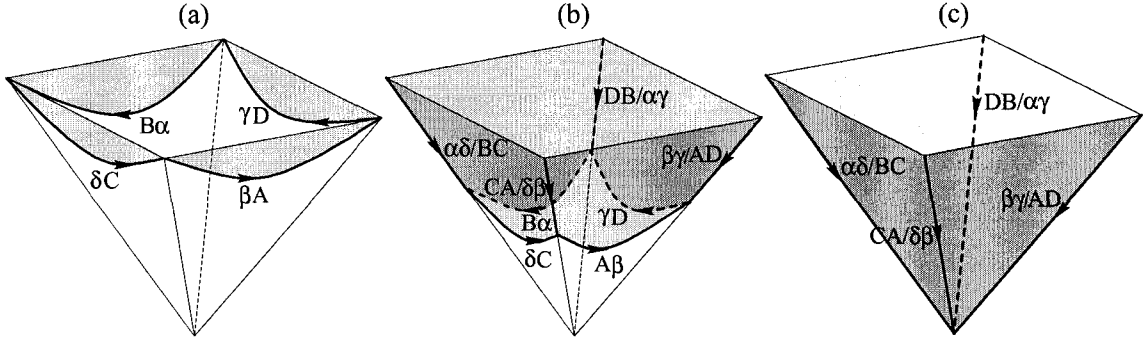
Figure 4.10   Various stages in the formation of the pyramidal defect structure.
Shaded regions represent intrinsic stacking faults. (a) nucleation and
glide of partials; (b) dislocation loop growth and zipping resulting in
sessile stair-rods; (c) pyramidal defect structure.

Dislocation glide: These partials, under the influence of the external stress due to indentation, glide away from the surface forming intrinsic faults on the slip planes.

Dislocation reaction: As the dislocation loops grow, the partials attract each other in pairs and zip to form sessile stair-rods along AC, AD, BD and BC according to the following reactions:

$$\delta C + \beta A = \delta\beta/CA$$

$$A\beta + D\gamma = AD/\beta\gamma$$

$$\gamma D + \alpha B = \gamma\alpha/DB$$

$$B\alpha + C\delta = BC/\alpha\delta \tag{4.7}$$

In vector notation the energetically favorable reactions are of the type

$$\tfrac{1}{6}[11\bar{2}] - \tfrac{1}{6}[\bar{1}1\bar{2}] = \tfrac{1}{3}[100] \tag{4.8}$$

The final defect, therefore, consists of a pyramid of intrinsic stacking faults on $\{111\}$ planes, which intersect the (001) surface with a four fold symmetry, and the $\langle 01\bar{1}\rangle$ edges of the pyramid consist of low energy sessile stair-rod dislocations. These sessile stair-rods act as barriers to further glide giving rise to the observed strain hardening during indentation beyond the first yield.

To examine the dependence of the defect structures on the orientation of the indenter with respect to the crystallographic axes of the gold substrate, the calculations were repeated with the edges of

the indenting face in (100) and (010) directions. The defect produced was similar to the pyramidal structure seen above where the high stresses at the corners of contact region nucleate partials on the four {111} planes. From the physics of the defect nucleation presented above, the above mechanism can be generalized to indentation of other {111} and {110} surfaces as well. It can be deduced that the indentation of {111} surface will produce a tetrahedral defect structure displaying the threefold symmetry observed in experiments [45]. And similarly the hexagonal nature of the indent produced by indenting the {110} surface is consistent with the proposed mechanism. Thus, the geometry of the defect structures is independent of the indenter orientation, but is a characteristic of the crystallography of the surface of the indented crystal.

4.4.1.3 Second Yield : Dislocation Locks

Further indentation results in a second yield, at which point dislocation loops are nucleated on the slip planes outside the defect as shown in Figure 4.11. Figure 4.12 shows the slip vectors s_{12}, of the atoms on the (111) plane dislocated during the second yield and the dislocation loops extending beyond the stair-rods can be seen. The contour plots of RSS on $(111)\langle 112\rangle$ along with the slip vectors are shown in Figure 4.13. It is seen that the activated slip direction is not along the maximum RSS direction, but along the direction in which the RSS has reached the critical value. This observation further corroborates the discussion presented above. Thus, deformation results through a sequence of elastic and plastic responses, with the elastic responses culminating in plastic events.

4.4.2 Retraction

When the indenter is retracted after the first yield point, the force curve retraces the indentation path at small displacements. This suggests that the defect nucleated at the first yield point has disappeared and the substrate has recovered is original undeformed state upon retraction. However, the force curve during retraction after the second yield point signifies permanent deformation.

Upon retracting the indenter, the external stress vanishes and the internal compressive stress dominates the dynamics of deformation. It is seen above that the interior of the pyramidal defect is under enormous compressive stress due to the strain imposed during the first yield. This compressive stress
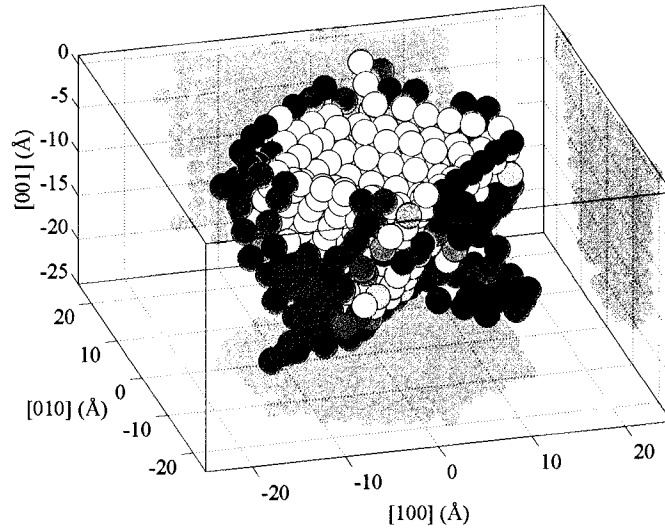
Figure 4.11 Deformed region illustrating the dislocation locks formed during the second yield. ○ represent the atoms that slipped during the first yield ($|s_{01}| > 0$) and light gray circles are the atoms that underwent slip during the second yield event ($|s_{12}| > 0$). Dislocation loops extend beyond the adjacent faces of defect structure forming dislocation locks.
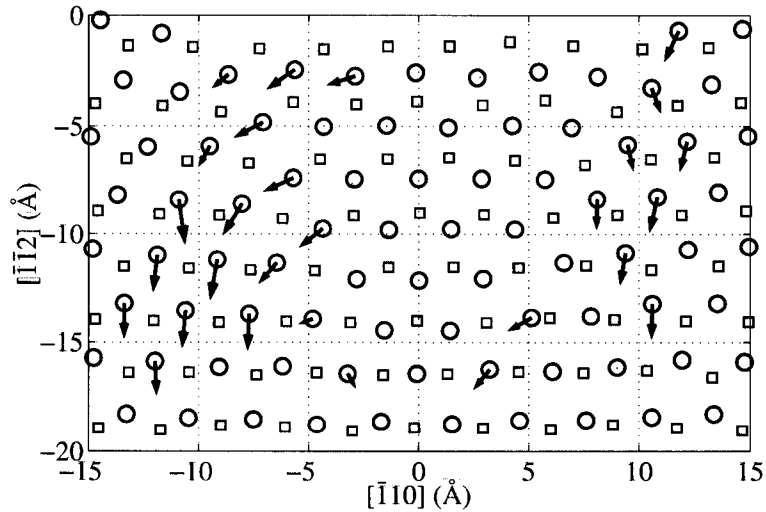
Figure 4.12 Slip vector s_{12} of the atoms on (111) plane. ○ represent the atoms of the slipped plane and □ represent the atoms of the unslipped plane adjacent to the slipped region. The slip is along the direction in which the resolved shear stress has attained the critical value.
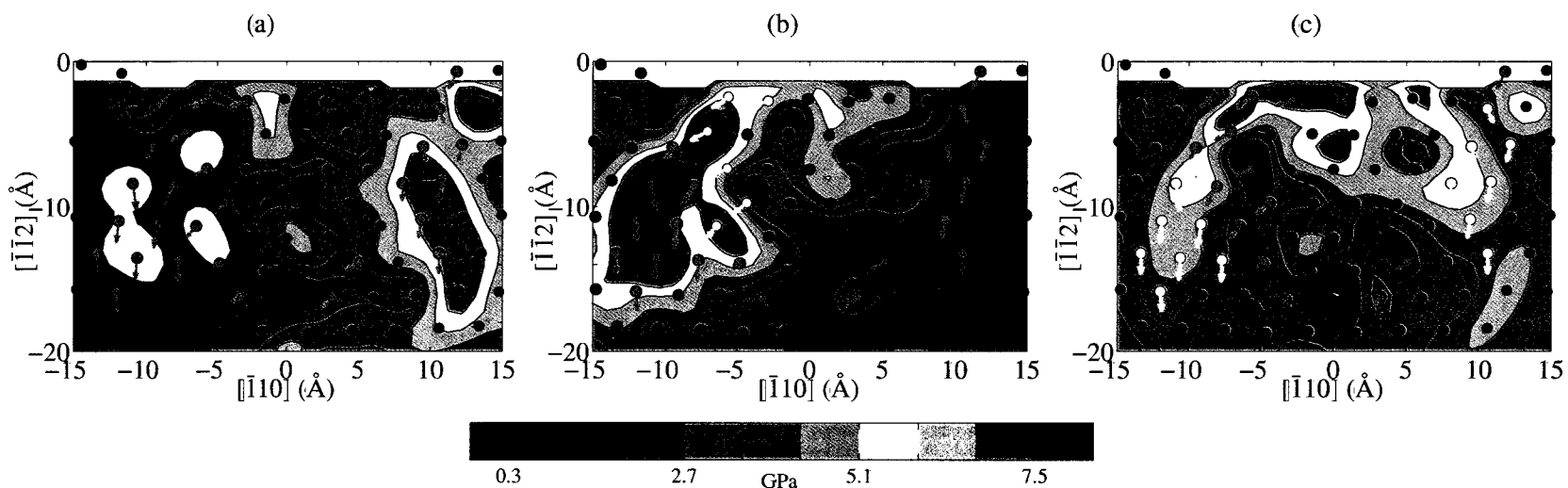
Figure 4.13 Resolved shear stresses on (111) plane, at the second yield point, along the direction: (a) $[12\bar{1}]$; (b) $[21\bar{1}]$; (c) $[11\bar{2}]$. ○ represent the atoms with slip vectors coinciding with the RSS direction; light gray circles represent other slipped atoms and ● represent the atoms in the undeformed region. The observed slip is not necessarily in direction of the maximum resolved shear stress.

when resolved onto the slip planes is opposite in direction to the RSS during indentation. A restoring force is induced that is strong enough to effect the unzipping of the stair-rods into their constituent partials, which then glide toward the surface healing the stacking fault along the way. Eventually, the defect disappears and the substrate recovers its original configuration with no residual deformation as seen in Figure 4.2.

However, after the second yield, the dislocation loops extend beyond the stair-rods leading to dislocation locking. And upon retracting the indenter after the second yield, the aforementioned restoring forces are not strong enough to unlock the locked structure, thus giving rise to permanent plastic deformation observed in Figure 4.2.

4.5 Concluding Remarks

We have investigated the atomistic mechanisms of plastic deformation during nanoindentation of Au (001) surface with a noninteracting indenter. A recently developed slip vector analysis has been employed to identify the defect structures formed during initial plastic yield. During indentation, the accumulated elastic energy in the indented region is partially relieved by the nucleation of a pyramidal defect structure. The defect is formed by the surface nucleation of Shockley partials on the four $\{111\}$ slip planes at the periphery of the contact region. These partials glide away from the surface creating stacking faults that grow in size and intersect with those on the adjacent planes. At the intersections, the partials zip to form sessile stair-rods which contribute to the strain hardening observed after the first yield. The observed slip is in the most energetically favorable direction, which corresponds to the direction in which the RSS has reached the critical value and is not necessarily the maximum value. The CRSS estimated in this study is in the range of $1.8 - 2.3$ GPa in excellent agreement with the experimental estimates.

Upon retracting the indenter after the first yield, the pressure due to the compressive strain in the defect induces restoring forces that heal the plastic deformation. Further indentation results in a second yield that causes the dislocation loops to extend beyond the stair-rods forming dislocation locks. The unlocking forces of these structures is greater than the internal restoring forces active during indenter retraction and thus effect permanent deformation after the second yield.

We proposed a three step mechanism based on dislocation theory that elucidates the physics behind the formation of the observed defect structures during gold nanoindentation. According to this mechanism, the defects produced depend on the crystallography of the indented surface as seen in experiments.

CHAPTER 5 THERMAL NON-CONTACT ATOMIC FORCE MICROSCOPY

Extended version of a paper to be submitted to *Physical Review Letters*

Anil Gannepalli [‡§], Abu Sebastian[‡], Jason C. Cleveland[¶] and Murti V. Salapaka[‡*]

5.1 Abstract

In this paper a new ambient temperature small amplitude frequency modulation (FM) technique is developed that uses the thermal noise response of the cantilever to estimate its resonant frequency [F. J. Giessibl, Jpn. J. Appl. Phys. I **33**, 3730 (1994)]. The dependence of cantilever's resonant frequency on the separation dependent tip-sample forces is utilized to maintain extremely small tip-sample separations by regulating the effective resonant frequency. This method is particularly suited for studying highly localized slowly evolving atomic or molecular phenomena. The experiments performed in ambient room conditions have achieved tip-sample separations less than 2 nm for time periods in excess of 30 min. At such small separations a force sensitivity of 14 fN in a bandwidth of 0.4 Hz is observed. This demonstrates a new thermal non-contact mode operation of AFM.

5.2 Introduction

In many studies a micro-cantilever based investigation of extremely small and local forces evolving over large time scales is of considerable interest. One such application is the detection of single electron spin where forces in the 10^{-14} N to 10^{-16} N have to be detected [9]. Another application is the study of biomolecular interaction dynamics [101, 102, 103, 104] that have timescales spanning from μs to

---

[‡]Department of Electrical and Computer Engineering, Iowa State University, Ames, IA 50011
[§]Primary researcher and author
[¶]Asylum Research, 341 Bollay Drive, Santa Barbara, CA 93117
[*]Author for correspondence, murti@iastate.edu

ms. In these applications in order to detect the highly localized forces it is essential to maintain a tip-sample separation on the order of Å to nm. In addition such separations have to be maintained with good separation stability for extended periods of time. This is a requirement imposed either by the time scales of the dynamic process being studied or the need to average to achieve the necessary sensitivity or both. In such studies the effect of the tip-sample contact on the dynamics is difficult to characterize and may be detrimental. This necessitates non-contact operation with extremely small rms tip deflections.

A primary hurdle for non-contact operation in static mode is the $1/f$-noise and drift of the system that becomes particularly detrimental over long time periods. Low temperatures can alleviate problems associated with low frequency noise but such conditions are not always conducive to the study. Furthermore, static mode methods cannot differentiate between attractive and repulsive interactions thereby making it incapable of maintaining the tip in the attractive regime. Classic dynamic methods overcome the above issues and are used in non-contact operation. However, they are associated with large amplitudes that are unacceptable. Moreover, the long-range forces encountered with large amplitudes reduce the sensitivity to short-range forces [35]. Consequently, small amplitude frequency modulation (FM-AFM) has been proposed [38] for true atomic resolution and considerable success has been demonstrated [105, 39]. However, the current FM technique based on positive feedback necessitates low temperature operation to suppress thermal vibrations. One method that has not received much attention since its mention [106], is the use of thermal vibrations of the cantilever in FM-AFM. Such a technique has the advantages of dynamic mode and small rms deflections of static mode.

In this study we develop the FM technique based on the thermal noise response of the cantilever that promises to meet the demands of maintaining sub-nanometer separations over large time periods. Such small separations facilitate the detection of forces on the order of 10 fN.

5.3 Theory and Model

The complex dynamics of the micro-cantilever is well modeled as a flexible structure with multiple modes. A first-mode approximation [107] as a simple damped harmonic oscillator is usually sufficient. Within this first-mode approximation the cantilever is modeled as a single spring-mass-damper system

free cantilever stiffness

tip-sample interactions
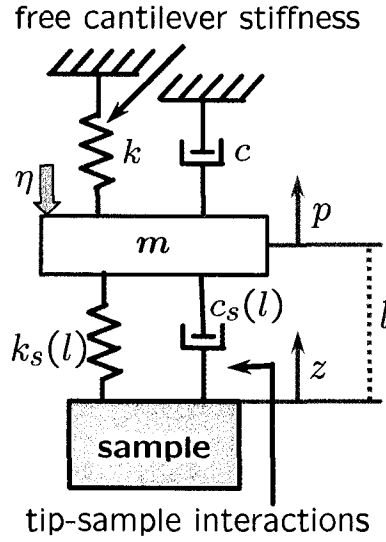
Figure 5.1 The cantilever is modeled by a spring-mass-damper system with a spring constant k, damping constant c and mass m. The tip-sample interactions are modeled as a sum total of conservative and dissipative forces. The distance dependence of these forces is accounted for by the nonlinear spring $k_s(l)$ and damper $c_s(l)$. η is the thermal forcing, p and z represent the motion of the cantilever and sample, respectively. l is the tip-sample separation.

(see Figure 5.1) as described by

$$m\ddot{p}(t) + c\dot{p}(t) + kp(t) = \eta(t) + F(t), \tag{5.1}$$

where $p(t)$ is the cantilever deflection, m is the mass of the cantilever, c is the damping constant, k is the spring constant and $\eta(t)$ is the Langevin thermal noise forcing term and $F(t)$ describes other external forces acting on the cantilever. In the absence of external forcing ($F(t) = 0$), taking Laplace transform of Equation (5.1) (assuming $p(0) = 0$) yields

$$\frac{p(s)}{\eta(s)} = H(s) = \frac{1}{ms^2 + cs + k}. \tag{5.2}$$

Therefore the power spectral density of $p(t)$ is given by [108]

$$P_{pp}(\omega) = |H(\omega)|^2 P_{\eta\eta}(\omega) \tag{5.3a}$$

$$= \frac{1}{(k - m\omega^2)^2 + c^2\omega^2} P_{\eta\eta}(\omega), \tag{5.3b}$$

where $P_{\eta\eta}(\omega)$ is the power spectral density of $\eta(t)$. Assuming $\eta(t)$ is white noise with constant spectral density $P_{\eta\eta}(\omega) = \sigma_\eta^2$, for a cantilever in thermal equilibrium, we have

$$
\begin{aligned}
\frac{1}{2}k_B T &= \frac{1}{2}k\langle p\rangle^2 \\
&= \frac{1}{2}k \int_0^\infty P_{pp}(\omega)d\omega \\
&= \frac{1}{2}k\sigma_\eta^2 \int_0^\infty \frac{1}{(k - m\omega^2)^2 + c^2\omega^2}d\omega,
\end{aligned}
\tag{5.4}
$$

where k_B is the Boltzmann's constant, T is the temperature. Solving for σ_η^2 [109], the thermal noise drive is

$$
\sigma_\eta^2 = \frac{4m\omega_0 k_B T}{Q},
\tag{5.5}
$$

and the spectral density of deflection of a cantilever in thermal equilibrium with no external forces is given by

$$
P_{pp}(\omega) = \frac{4\omega_0 k_B T}{Qm} \frac{1}{(\omega_0^2 - \omega^2)^2 + (\frac{\omega_0\omega}{Q})^2}.
\tag{5.6}
$$

The resonant frequency is given by

$$
\omega_R = \omega_0 \sqrt{1 - \frac{1}{4Q^2}},
\tag{5.7}
$$

where ω_0 $(= \sqrt{k/m})$ is the undamped resonant frequency and Q $(= \frac{\omega_0 m}{c})$ is the quality factor of the cantilever.

When the tip interacts with the sample, the tip-sample forces $(F(t) = F_s(t))$ alter the cantilever dynamics. The tip-sample forces can be modeled as a spring-damper system (see Figure 5.1) by separating the conservative and dissipative interactions as

$$
F_s(l(t), \dot{l}(t)) = -k_s(l)l(t) - c_s(l)\dot{l}(t),
\tag{5.8}
$$

where k_s $\left(= -\frac{\partial F_s}{\partial l}\Big|_l\right)$ is the force gradient and c_s $\left(= -\frac{\partial F_s}{\partial \dot{l}}\Big|_l\right)$ accounts for the dissipation induced by tip-sample interactions. In such a scenario the changes in the cantilever dynamics can be analyzed by linearizing about an equilibrium state (denoted by $*$) as below

$$
m\ddot{\delta p}(t) + c\dot{\delta p}(t) + k\delta p(t) = \eta(t) - c_s^*\dot{\delta l}(t) - k_s^*\delta l(t)
\tag{5.9}
$$

where $\delta z(t) = z(t) - z^*$, $\delta l(t) = l(t) - l^*$, $\delta p(t) = p(t) - p^*$ are the deviation variables. Observing $\delta l = \delta p - \delta z$ from Figure 5.1 it follows that

$$
m\ddot{\delta p}(t) + c_{\mathit{eff}}\dot{\delta p}(t) + k_{\mathit{eff}}\delta p(t) = \eta(t) + c_s^*\dot{\delta z}(t) + k_s^*\delta z(t)
\tag{5.10}
$$

where k_{eff} $(= k + k_s^*)$ is the effective spring constant and c_{eff} $(= c + c_s^*)$ is the effective damping constant. Therefore, the tip-sample interactions have the effect of altering the effective spring and damping constant thereby changing the resonant frequency of the cantilever. For small tip-sample forces the resonant frequency shift $\Delta\omega_R$ can be approximated by the relation

$$\frac{\Delta\omega_R}{\omega_R} \approx \left(\frac{\omega_0^2}{\omega_R^2}\right)\frac{k_s^*}{2k} - \left(\frac{\omega_0^2}{\omega_R^2} - 1\right)\frac{c_s^*}{c}. \tag{5.11}$$

In the above equation the first and second term on the right represent the contributions of the conservative and dissipative interactions to the frequency shift. It is therefore possible to separate the conservative and dissipative tip-sample interactions from the cantilevers thermal noise response. The total frequency change can be estimated from the shift in the peak position and the broadening of the peak quantifies dissipative interactions. For large Q and negligible near surface damping, the frequency change is primarily due to the conservative forces as shown below

$$\Delta\omega_R \approx \omega_R\frac{k_s^*}{2k}. \tag{5.12}$$

The effective resonant frequency $\omega_{R,eff}$ $(= \omega_R + \Delta\omega_R)$ decreases (increases) when the tip-sample interaction force is attractive (repulsive). Thus, by observing the effective resonant frequency the attractive and repulsive regimes of the interaction potential can be differentiated. The information about $\omega_{R,eff}$ is available in the power spectral density of the thermal noise response as a shift in the peak position of the spectral density. In this work this fact is utilized to control the tip-sample separation by regulating the effective resonant frequency. One essential requirement is that the cantilever spring constant be large enough to avoid any jump-to-contact instabilities in the region of operation $(k + k_s^* > 0$ for all $l^*)$.

5.4 Control Scheme: Systems View

Maintaining a constant tip-sample separation translates into a problem of regulating the effective resonant frequency of the cantilever at a desired value as illustrated in the proposed control architecture in Figure 5.2. For a high Q cantilever, its thermal noise response as observed in the deflection signal is assumed to be a single sinusoid in white noise. The frequency of this sinusoid, corresponding to
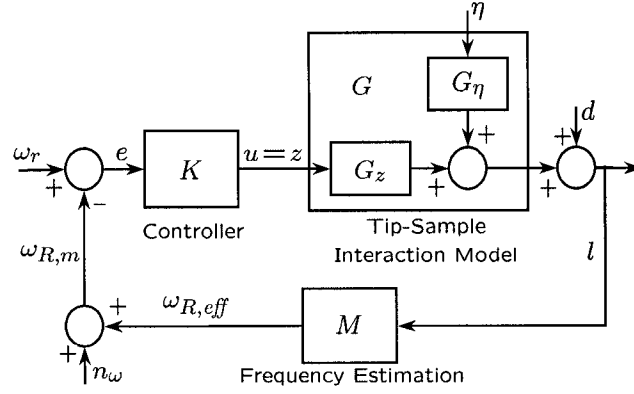
Figure 5.2 Systems view of the closed loop. G refers to the cantilever interact-
ing with the sample and consists of the transfer functions $G_z(s)$ and
$G_\eta(s)$. $G_z(s)$ accounts for the dependence of the tip-sample separa-
tion l on the sample position z and $G_\eta(s)$ represents the effect of η on
l. $M(s)$ represents the dependence of $\omega_{R,eff}$ on l. $K(s)$ is the feed-
back control law actuating the z-motion of the sample, via the control
output u, in an effort to maintain the measured resonant frequency ω_m
at the desired value ω_r. n_ω represents the noise in the frequency esti-
mation. The effect of the drift processes is modeled as a disturbance d
in the sample position.

the effective resonant frequency of the cantilever, is estimated by Pisarenko harmonic decomposition
(PHD) [110].

The block G refers to the cantilever interacting with the sample and consists of the transfer functions

$G_z(s)$ and $G_\eta(s)$. $G_z(s)$ accounts for the dependence of the tip-sample separation l on the sample

position z and $G_\eta(s)$ represents the effect of η on l. Expression for these transfer functions can be

derived by rewriting Equation (5.9) in terms of δl and δz as,

$$m\ddot{\delta l}(t) + c_{eff}\dot{\delta l}(t) + k_{eff}\delta l(t) = \eta(t) + m\ddot{\delta z}(t) + c\dot{\delta z}(t) + k\delta z(t). \tag{5.13}$$

Taking Laplace transform (assuming $\delta l(0) = \delta z(0) = 0$) and rearranging we get

$$\delta l(s) = G_z(s)\delta z(s) + G_\eta(s)\eta(s), \tag{5.14a}$$

$$G_z(s) = \frac{-(ms^2 + cs + k)}{ms^2 + c_{eff}s + k_{eff}}, \tag{5.14b}$$

$$G_\eta(s) = \frac{1}{ms^2 + c_{eff}s + k_{eff}}. \tag{5.14c}$$

$M(s)$ represents the dependence of $\omega_{R,eff}$ on l. For small variations in l, $M(s)$ can be approximated

by a simple gain as

$$M(s) = M^* = \left. \frac{\partial \omega_{R,\text{eff}}}{\partial l} \right|_{l^*}.$$ (5.15)

$K(s)$ is the feedback control law actuating the z-motion of the sample, via the control output u, in an effort to maintain the measured resonant frequency ω_m at the desired value ω_r. n_ω represents the noise in the frequency estimation. The effect of the drift processes is modeled as a disturbance d in the sample position.

In order to maintain a constant l the control scheme should be capable of compensating for the disturbances d. Additionally, for good resolution the effect of the frequency noise n_ω on l should be minimal. These dependencies can be evaluated from the following closed loop equation

$$l(s) = \frac{1}{1 + G_z(s)K(s)M(s)}d(s) + \frac{G_z(s)K(s)}{1 + G_z(s)K(s)M(s)}\omega_r - \frac{G_z(s)K(s)}{1 + G_z(s)K(s)M(s)}n_\omega(s).$$ (5.16)

From Equation (5.15) the closed loop response is rewritten as

$$l(s) = S(s)d(s) + T(s)\frac{\omega_r(s)}{M^*} + T\frac{n_\omega(s)}{M^*}.$$ (5.17)

where $S(s) = \frac{1}{1+G_z(s)K(s)M(s)}$ and $T(s) = \frac{G_z(s)K(s)M(s)}{1+G_z(s)K(s)M(s)}$ are the closed loop transfer functions from d to l and n_ω and l, respectively. S is the sensitivity transfer function that needs to be small in the frequency band where disturbances are present for good disturbance rejection. T is the complementary sensitivity function that needs to be small so as to minimize the effects of noise. Therefore, S is a measure of the bandwidth and T is a measure of resolution. Since,

$$S(j\omega) + T(j\omega) = 1,$$ (5.18)

$|T(j\omega)|$ has to be large when $|S(j\omega)|$ is small and vice-versa. Hence, these transfer functions capture the classic trade off between bandwidth and resolution. The closed loop bandwidth B is defined as the frequency at which $|S(j\omega)|$ crosses -3 dB from below. Therefore, the controller K should be designed such that

$$|S(j\omega)| \quad < \quad 1, \ \omega < \omega_B$$ (5.19a)

$$|T(j\omega)| \quad \begin{cases} = & 1, \ \omega \leq \omega_T (\approx \omega_B) \\ \\ \ll & 1, \ \omega > \omega_T \end{cases},$$ (5.19b)

where $\omega_B = 2\pi B$ is the upper bound on the bandwidth of d.

Any other disturbance in the tip-sample forces that has a bandwidth greater than the closed loop bandwidth of the system B, will not be acted upon by the controller and will potentially show up as a variation in the cantilever's resonance. This is the principle behind the use of this technique to monitor variations in tip-sample interaction forces. Therefore, for imaging the controller should be designed such that the closed loop bandwidth is intermediate to that of the disturbance and the imaging signal.

5.5 Sensitivity and Resolution

5.5.1 Sensitivity

The sensitivity, measured in terms of minimum detectable frequency change, is limited by the frequency noise n_ω. The two frequency noise sources in this scheme are: (1) thermal fluctuations of the cantilever, (2) noise in the deflection sensor.

For a cantilever in thermal equilibrium the thermal limit for the frequency resolution, in a bandwidth B, is given by [111]

$$\sigma_{\omega_{th}}^2 = \frac{B\omega_0}{2Q}. \tag{5.20}$$

This represents a lower limit of the frequency noise due to thermal vibrations. Since the thermal excitation is the signal source, the absence of cantilever spring constant k and temperature T in Equation(5.20) is expected. This makes thermal FM operation possible at room temperature.

Frequency noise due to the displacement sensor with a noise density ρ_{DS} in a bandwidth B is (see [112])

$$\sigma_{\omega_{DS}}^2 = \frac{\rho_{DS} k B^3}{\pi^2 k_B T}. \tag{5.21}$$

For displacement sensors, like the shot noise limited photodiode [18] used in this study, $\rho_{DS} \approx 10^{-6} \text{ Å}^2/\text{Hz}$.

The above two sources of noise provide a lower limit of the frequency noise in this scheme. However, in practice the frequency estimates have a higher noise density represented by ρ_ω. The sensitivity in a bandwidth B is then given by

$$\sigma_\omega = n_\omega = \sqrt{\rho_\omega B}. \tag{5.22}$$

5.5.2 Vertical Resolution

The vertical resolution, defined as the smallest change in tip-sample separation that can be resolved, is limited by the noise in the tip-sample separation. The two major sources of vertical noise are (1) fluctuations in sample position σ_z^2 and (2) thermal fluctuations of the cantilever $\sigma_{p_{th}}^2$.

The noise in sample position is a consequence of the frequency noise being fed back in the control scheme. The transfer function between δz and n_ω from Figure 5.2 is

$$\delta z(s) = -\frac{K(s)}{1 + G_z(s)M(s)K(s)}n_\omega(s). \tag{5.23}$$

Equation (5.14a) can therefore be rewritten as

$$\delta l(s) = -\frac{G_z(s)K(s)}{1 + G_z(s)M(s)K(s)}n_\omega(s) + G_\eta(s)\eta(s). \tag{5.24}$$

Recognizing $\frac{G_z(s)K(s)}{1+G_z(s)M(s)K(s)} = \frac{1}{M^*}T(s)$, the power spectral density of $\delta l(t)$, when $n_\omega(t)$ and $\eta(t)$ are statistically independent, is given by

$$P_{ll}(\omega) = \frac{1}{M^{*2}}|T(j\omega)|^2 P_{\omega\omega}(\omega) + |G_\eta(j\omega)|^2 P_{\eta\eta}(\omega). \tag{5.25}$$

where $P_{\omega\omega}(\omega)$ and $P_{\eta\eta}(\omega)$ are the power spectral densities of $n_\omega(t)$ and $\eta(t)$ respectively.

For a bandwidth B and frequency noise density ρ_ω, the vertical noise is

$$\begin{aligned} \sigma_l^2 = \langle \delta l^2 \rangle &= \frac{1}{2\pi}\int_0^{\omega_B} P_{ll}(\omega)d\omega \\ &= \frac{\rho_\omega}{2\pi M^{*2}}\int_0^{\omega_B}|T(j\omega)|^2 d\omega + \frac{1}{2\pi}\int_0^{\omega_B}|G_\eta(\omega)|^2 P_{\eta\eta}(\omega)d\omega, \end{aligned} \tag{5.26}$$

where $|G_\eta(\omega)| \approx \frac{1}{k_{eff}}$, $\omega_B \ll \omega_R$ and $|T(j\omega)| \approx 1$, $\omega < \omega_B$. Substituting $M(\omega) = M^*$ and $P_{\eta\eta}(\omega) = 4m\omega_0 k_B T/Q$ the expression for vertical noise reduces to

$$\begin{aligned} \sigma_l^2 &= \frac{\rho_\omega}{M^{*2}}B + \frac{4m\omega_0 k_B T}{k_{eff}Q}B \\ &= \frac{\rho_\omega}{M^{*2}}B + \frac{4m k_B T}{\omega_0 Q}B, \text{ for } k_{eff} \approx k. \end{aligned} \tag{5.27}$$

This clearly illustrates the trade off between bandwidth and resolution where a smaller B gives better sensitivity and resolution.

5.6 Thermal FM versus Classical FM

In classical FM where the amplitudes are large ($A \approx 10$nm) changes in the cantilever's resonance are due to both the long-range and short-range tip-sample forces. This limits the ability to observe localized phenomena on the sample surface. Since the tip-sample forces are highly nonlinear, the observed frequency shifts have a complex dependence on the tip-sample forces encountered throughout the trajectory of the tip [35, 36]. Therefore the interpretation of the data is non-trivial and requires an involved deconvolution procedure [37]. Furthermore, larger the amplitude, smaller the frequency shifts because the tip interacts with the sample for a smaller fraction of the oscillation period. However, the frequency noise decreases with larger amplitudes as $n_\omega \propto A^{-2}$ (see [28]). An optimal signal-to-noise (S/N) ratio is reached for rms deflections on the order of the decay lengths of the short-range forces [38]. Small amplitudes filter off the long-range contributions to the imaging signal thereby increasing the sensitivity to short-range forces. In addition, the interpretation of the observed changes in cantilever dynamics is straightforward as seen in Section 5.3.

The jump-to-contact instability in small amplitude operation necessitates the use of stiff cantilevers. Current FM technique based on positive feedback also requires low temperature operation for improved S/N ratios by suppressing the thermal vibrations of the cantilever. Thermal FM technique proposed in this work uses thermal excitation of the cantilever, thus eliminating the need for positive feedback and making the operation possible at ambient temperatures. However, this also results in significant amount of frequency noise that restricts the operational bandwidth for a desired sensitivity.

5.7 Experimental Results

The thermal noise based non-contact mode operation is demonstrated in a variety of experiments few of which are discussed below. The experiments are performed on a Digital Instruments Multimode AFM in ambient environment. The signal processing for frequency estimation and the controller are implemented on a TMS320C44 digital processing platform. Silicon cantilevers with a nominal $Q = 450, k = 1$ N/m and $\omega_R = 350$ kHz are used with freshly cleaved HOPG. Since the variance of PHD estimates scales with the square of the frequency, the deflection signal was frequency modulated such that the frequency of the peak spectral density is around 5 kHz. The frequency estimates are available
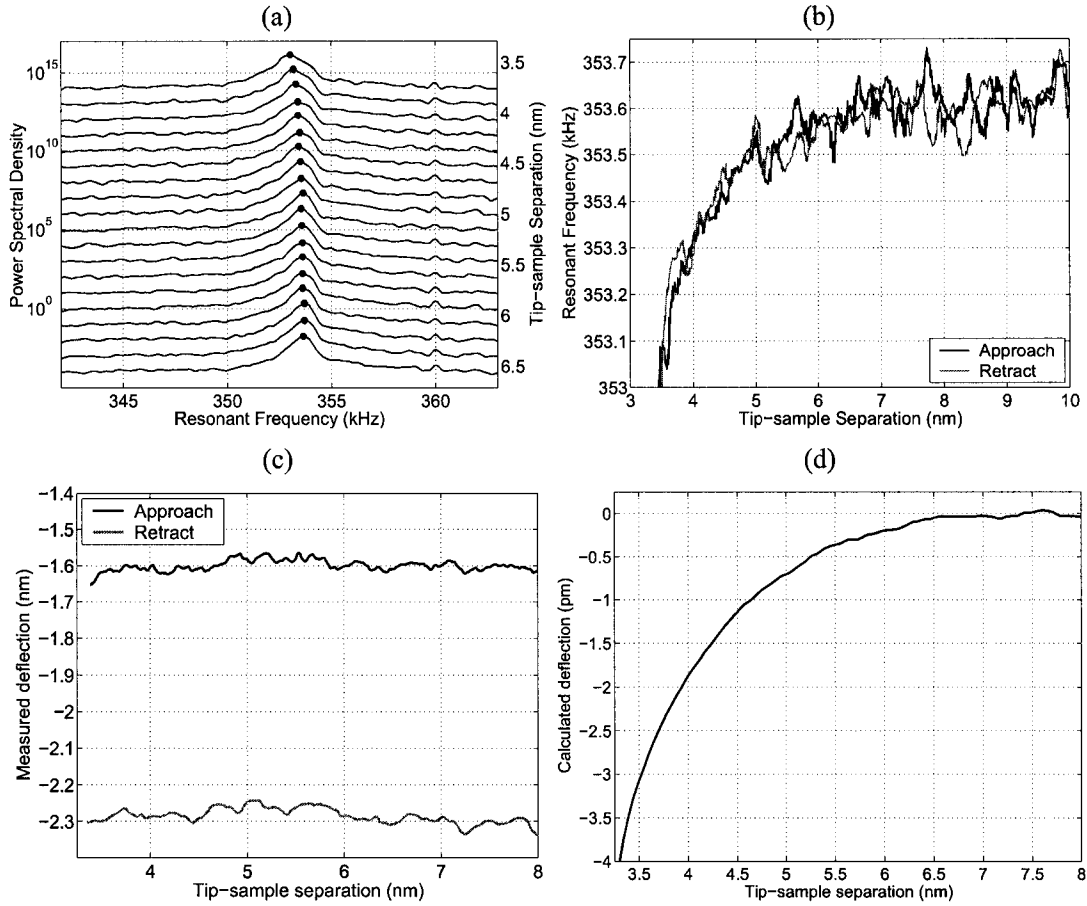
Figure 5.3 (a) The effect of tip-sample forces on the cantilever's thermal noise re-
sponse. As the tip-sample separation reduces, the peak position shifts
towards lower frequencies due to the attractive forces. (b) The cor-
responding variation observed in the frequency estimates during ap-
proach and retract phases of a force curve. (c) The variations in de-
flection show no indication of any attractive forces. (d) Calculated
deflection $p_{calc} = \frac{2}{\omega_0} \int \Delta\omega dl$ (see Equation (5.12)) for the frequency
changes observed in (b). The maximum calculated deflection of 4 pm
is much smaller than the deflection sensitivity of the instrument at low
bandwidths. The noise in the deflection signal at such low bandwidths
is $\approx$ 1 Å.

at a bandwidth of 265 Hz with a noise density $\rho_\omega \approx 600$ Hz^2/Hz. The observed noise in deflection sensor is $\rho_{DS} = 10^{-6}$ Hz^2/Hz. For these experimental parameters the total theoretical lower limit for the frequency noise calculated from Equations (5.20) and (5.21) is about 400 Hz^2/Hz. The observed frequency noise is significantly higher due to the algorithmic deficiencies in implementation that can be significantly improved in future.

Figure 5.3(a) shows the observed changes in the thermal noise response of the cantilever as it interacts with the sample. In Figure 5.3(b) the variation in the estimated cantilever's resonant frequency as a function of tip-sample separation during approach and retraction is shown. It is seen that the resonant frequency decreases due to the long-range attractive tip-sample interactions. The strength of these attractive forces increases with a decreasing tip-sample separation. However, a similar effect is not observed in the deflection as the maximum observable deflection (see Figure 5.3(c)) estimated to be approximately 4 pm is much smaller than the deflection sensitivity of the instrument at low bandwidths.

5.7.1 Non-contact Mode Operation

The following experiment demonstrates the feasibility of the proposed method to control the tip-sample separation. In this experiment the control scheme is made to track a step change in the reference frequency. The cantilever resonant frequency estimates, control signal and deflections are shown in Figures 5.4(a), 5.4(b) and 5.4(c), respectively. In the initial stages of the control, the tip is not interacting with the sample and the measured resonance is 353.6 kHz (see Figure 5.4(a)), which is the free resonant frequency of the cantilever. The controller, therefore, acts to move the sample towards the tip as seen in Figure 5.4(b). Once the desired tip-sample separation is achieved, indicated by the resonant frequency being close to the reference, the control action counteracts the drift in the instrument. At approximately 1600 s into the experiment the step change in the reference is introduced and the controller is able to track this change. As the reference is reduced, implying a smaller desired tip-sample separation, the controller moves the sample towards the tip and is seen as a small "spike" in Figure 5.4(d) at 1600 s. This control action results in a reduction in tip-sample separation from about 7.1 nm to 6.3 nm as seen in Figure 5.4(e). The new reference is reached in less than 1 s. As reasoned earlier, the variations in deflection in Figure 5.4(c) can be attributed to the drift as the tip-sample forces are too small to induce
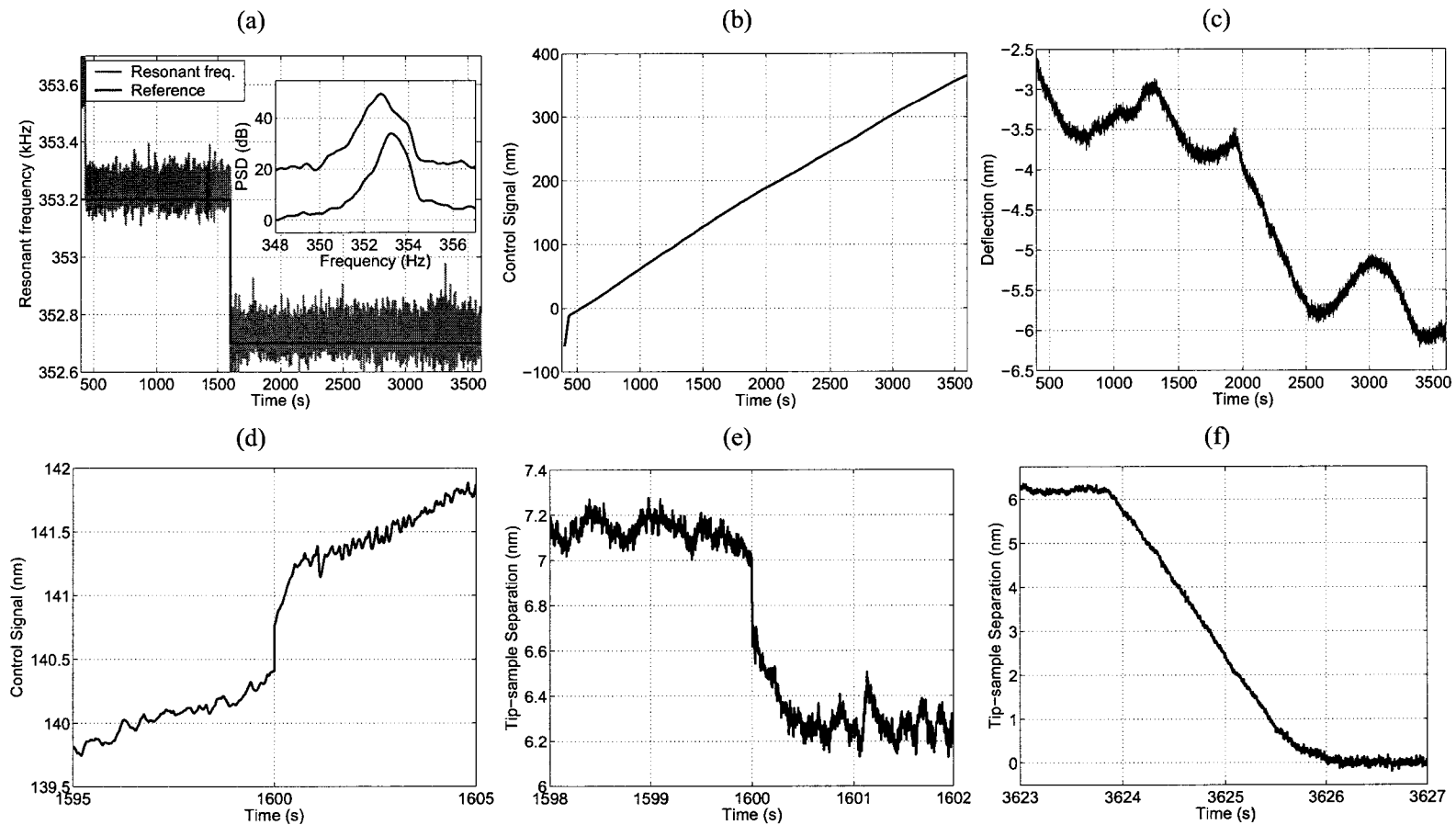
Figure 5.4 Time histories of (a) estimated frequency (b) control effort and (c) deflection while tracking a step change in reference frequency in non-contact mode. Successful tracking of the step in reference at 1600 s is seen in (a). Inset in (a) shows the shift in the peak positions of the spectra before and after the step change. Control effort in (b) indicates a significant amount of drift that is effectively compensated by the controller. The variations in deflection observed in (c) are attributed to the drift in the deflection sensor or thermal bending of the cantilever. The response of the closed loop to the step change as seen in (d) control effort and (e) tip-sample separation. (f) Assuming the effects of drift are negligible in a small time window, the tip-sample separation is estimated to be 6.3 nm. The tip-sample contact is used as a 0 nm reference.

any perceivable change in the deflection. As seen in the control signal and the cantilever deflection, the instrument is afflicted with significant drift at room temperatures. This makes non-contact mode operation for long time periods virtually impossible in static mode. Figure 5.4(f) shows that the tip-sample distance of about 6.3 nm is maintained for over 30 mins until the experiment was terminated.

It is interesting to note that a separation of 6.3 nm doesn't agree with the corresponding separation for a resonant frequency of 352.7 kHz in Figure 5.3(b). This discrepancy can be attributed to the changes in the tip-sample interactions due to the adsorption of moisture and other adsorbates in ambient air on the sample surface during the long time duration ($>$ 1 hour) of the experiment. Therefore, a more accurate description of tip-sample interactions will be given by the resonant frequency dependence immediately after the experiment. Figure 5.5 shows the current state of the tip-sample interactions and it can be seen that a resonant frequency of 352.7 kHz does indeed correspond to a tip-sample separation of about 6.3 nm. Therefore, it is more accurate to refer to the surface contamination as the sample and the true tip-sample separation can be estimated by fitting a van der Waals type force to the observed force dependence on the tip-sample separation.
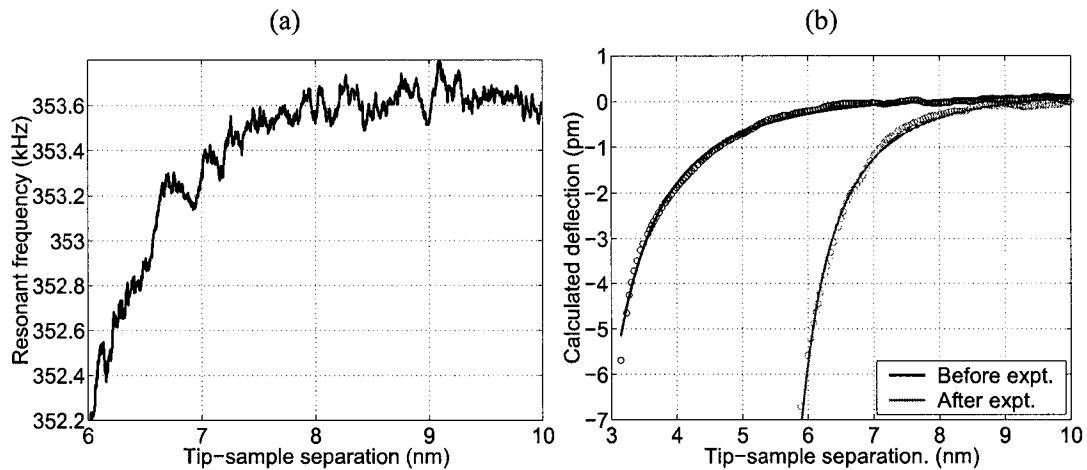
Figure 5.5   (a) Updated dependence of the resonant frequency on the tip-sample separation (b) Calculated cantilever deflections before and after the experiment are shown as circles. A van der Waals type force fit to the deflections is shown as solid lines. The fits estimate a thickness of the surface contamination to be $l_0 \approx 1.6$ nm at the beginning of the experiment. The thickness of this layer increases to $l_0 \approx 4.9$ nm by the end of the hour long experiment. Therefore the true tip-sample separation is $l' \approx 1.4$ nm throughout the experiment.

For a sphere plane geometry, the dependence of van der Waals forces on the separation l' is well approximated by

$$F_{vdW} \propto \frac{1}{l'^2(l'+R)^2}, \text{ for } l' < R, \tag{5.28}$$

where R is the tip radius. l' is the true tip-sample separation between the tip and the contaminants on HOPG surface such that $l' = l - l_0$, where l is the separation between the tip and HOPG surface, and l_0 is the thickness of the surface contamination. For the quasi-static experiments $F_{vdW} = k_{eff}p_{calc}$ where $k_{eff} \approx k$ because $\Delta\omega_R << \omega_R$. Consequently, p_{calc} will have the same dependence on l' as F_{vdW}. Figure 5.5(b) shows van der Waals force fits to the deflections calculated from the observed resonant frequency versus separation before (Figure 5.3(b)) and after (Figure 5.5(a)) the experiment. With a tip-radius of 10 nm the contaminant layer thickness l_0 is estimated at 1.6 nm and 4.9 nm before and after the experiment respectively. The values of l_0 are fairly insensitive to the magnitude of R. This yields a true tip-sample separation $l' \approx 1.4$ nm throughout the experiment. In addition, a change of 0.8 nm in the tip-sample separation (see Figure 5.4(e)) induced by a step change in the reference correlates well with the change required for a reduction in the resonance from 353.2 kHz to 352.7 kHz in Figure 5.5(a).

5.7.2 Non-contact Mode Imaging

Figure 5.6 demonstrates the non-contact imaging capability of this method. In this experiment the force gradient is modulated by moving the sample in a sinusoidal manner while the tip-sample separation in being maintained. The resonant frequency of the cantilever in Figure 5.6(a) during control is lower than its free resonance signifying non-contact mode of operation. The drift compensation seen in Figure 5.6(b) indicates that a separation of 4.2 nm (see Figure 5.6(c)), between the tip and HOPG surface, is maintained for the duration of the experiment (30 mins). During control the sample position is modulated by a 0.125 − 2 Å, 250 Hz sine wave such that the modulation frequency is greater than the closed-loop bandwidth (1.4 Hz as seen later) and hence will not be acted upon by the controller. This results in a modulation of the tip-sample separation and consequently the cantilever's resonance modulates at 250 Hz for modulation amplitudes as small as 0.25 Å as seen in Figure 5.6(d). No signature of this modulation is seen in the deflection signal (see Figure 5.6(e)) until the modulations are
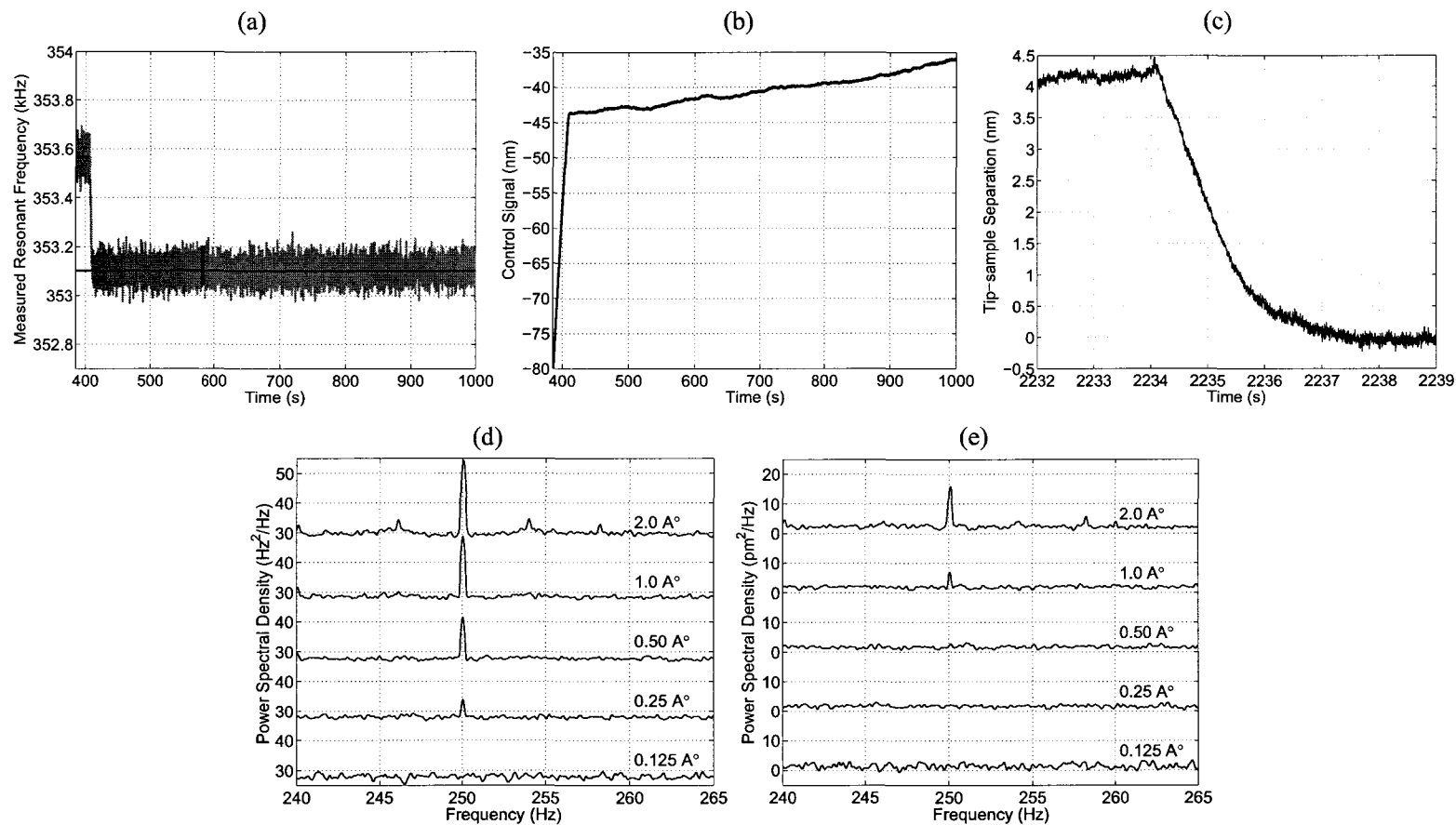
Figure 5.6 (a) Cantilever's natural resonance is at 353.6 kHz. A lower resonant frequency (353.1 kHz) during control indicates non-contact mode operation. (b) The tip is maintained at a separation of 4.2 nm from the sample for 30 mins. (c) Drift compensation by the controller. (d) Power spectral density plots of the resonant frequency estimates. A modulation of the resonant frequency at 250 Hz is observed for tip-sample separation modulation amplitudes as small as 0.25 Å. (e) Power spectral density plot of cantilever deflection. No modulation in the deflection is observed until the signal amplitude is 1 Å.

as large as 1 Å. Therefore, the resolution of resonance frequency is 4 times that of the deflection. It should however be noted that the imaging signal was detected in the deflection measurements because the thermal non-contact mode is able to eliminate the drift and maintain a constant tip-sample separation. In static mode operation this would be virtually impossible at ambient temperatures. Furthermore, for imaging signals with a lower bandwidth $1/f$ noise will deteriorate the resolution of the deflection measurements.

5.7.3 Bandwidth, Sensitivity and Resolution
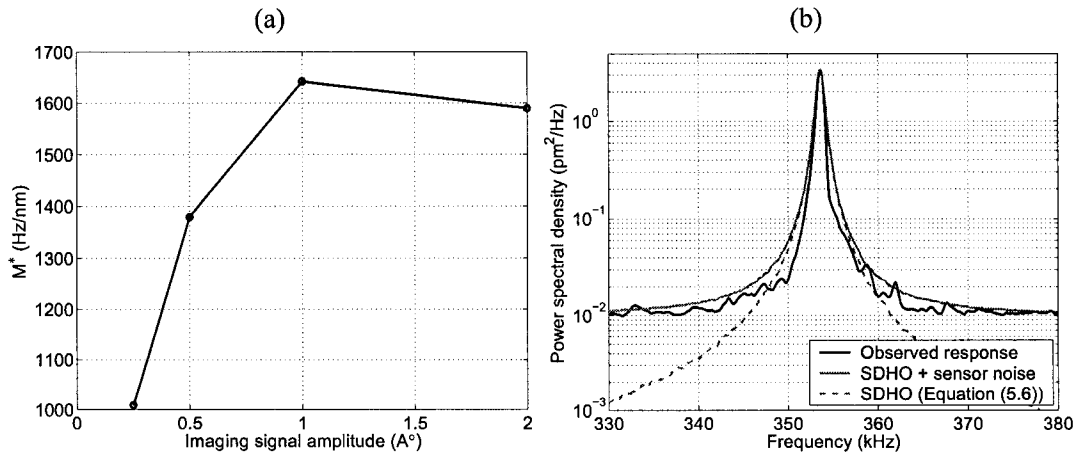
Figure 5.7 (a) $M^* = \frac{\Delta \omega_R}{\Delta l}$ evaluated by estimating the magnitude of the signal at 250 Hz in Figure 5.6(e) for various modulation amplitudes. (b) Cantilever parameter estimation by fitting the response of a simple damped harmonic oscillator (SDHO) with deflection measurement noise to the thermal noise response of the cantilever. The fit shown in the plot yields a SDHO with $k \approx 1$ N/m, $Q \approx 437$ and $\omega_R \approx 353.6$ kHz.

The dependence of $\omega_{R,eff}$ on l represented by M^* can be determined by estimating the frequency change as the area under the peak of the spectral densities in Figure 5.6(e). The estimates of M^* are plotted in Figure 5.7(a). A nominal value of $M^* = 1000$ Hz/nm corresponding to the smallest detectable imaging signal is used to estimate the performance limits. The cantilever properties are estimated by fitting the response of a single damped harmonic oscillator (SDHO) with sensor noise to the thermal noise response of the cantilever as shown in Figure 5.7(b). The values of $k = 1$ N/m, $Q = 437$ and $\omega_0 \approx \omega_R = 2.222 \times 10^3$ rad/s (353.6 kHz) are used to evaluate the closed loop transfer

functions shown in Figure 5.8. The closed loop bandwidth is estimated to be $B = 1.4$ Hz. Therefore, the sensitivity of the control loop is $\sigma_\omega \approx 29$ Hz and the resolution is $\sigma_l \approx 29$ pm.
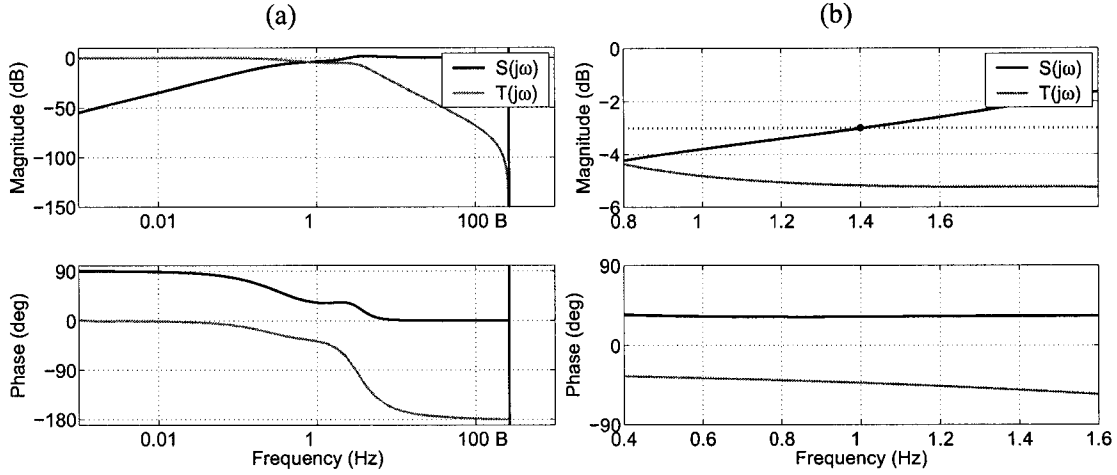

Figure 5.8   (a) Bode plots of the closed loop transfer functions $S(j\omega)$ and $T(j\omega)$.
(b) Closed loop bandwidth (defined as the frequency at which $|S(j\omega)|$ crosses -3 dB from below) is estimated to be $B \approx 1.4$ nm.

In Section 5.7.2 the imaging signal has a frequency of 250 Hz, but the bandwidth of the signal is 0.4 Hz (peak width in Figure 5.6(a)). In such a narrowband imaging scenario the sensitivity and resolution are 15.5 Hz and 15.5 pm. Therefore, a signal with an amplitude of 0.125 Å (17.7 pm rms) that is marginally greater than the vertical resolution is not detected. The magnitude of changes in the tip-sample force due to the 0.25 Å ($\Delta l = 50$ pm) signal that results in a frequency variation of $\Delta \omega$ ($= M^* \Delta l$) $= 50$ Hz is $\Delta F_s = \frac{2k}{\omega_R} \Delta \omega \Delta l \approx 14$ fN. Similarly for the 1 Å signal ($M^* = 1640$ Hz/nm) the force variation is 371 fN. Therefore, the frequency measurements are 25 times as sensitive as the deflection measurements.

5.8 Concluding Remarks

A new thermal non-contact mode of operation of AFM based on the thermal noise response of the cantilever is demonstrated. In this approach, cantilever's thermal noise response is used to estimate the changes in its resonant frequency that are fed back for maintaining the tip-sample separation. This method enables an extremely powerful small non-contact imaging technique in FM mode at room

temperatures. Tip-sample separations as small as 1.4 nm for periods extending over 30 min have been achieved. A force sensitivity of 14 fN in a bandwidth of 0.4 Hz is observed. Imaging of a 250 Hz narrowband signal is demonstrated in experiments performed in ambient room conditions.

In its current state, thermal non-contact AFM is severely limited in bandwidth because of significant amount of noise in the experimental setup. Better design of the instrument and controlled conditions along with advanced frequency estimation algorithms [113] hold the promise of enhanced performance of this technology.

CHAPTER 6 CONCLUSIONS AND FUTURE DIRECTIONS

Micro-cantilever based scanning probe technology has significantly enhanced the experimental capability to probe and modify matter at the nanoscale. However, it is still severely limited in achieving the bandwidths, sensitivity and resolution necessary for Nanotechnology. This thesis takes a complementary approach involving theoretical investigations and experimental advances to study the effects of the tip-sample forces in an AFM on the sample deformation and cantilever dynamics.

Atomistic processes involved in nanomodification of materials are inaccessible to experimental observation and theoretical methods provide a convenient way to study them. Molecular dynamics simulations are used to study the mechanics of plastic deformation and defect formation during nanoindentation of crystalline silicon and gold. A new approach based on a local strain diagnostic is presented to identify plastic rearrangements in silicon. During indentation, both the substrates show an elastic response indicated by a build up of von Mises stress which is relieved via a plastic deformation after a critical value is reached. However, the nature of deformation is very different. Silicon undergoes amorphization via a densification transformation by the formation of interstitials. In gold a pyramid shaped defect is formed that agrees with experimental observations. A three step mechanism for the defect formation is proposed that involves the nucleation, glide and reaction of dislocations. Permanent deformation in gold is a result of the formation of dislocation locks that require large unlocking forces. Experimentally observed defect structures, force curve hysteresis and strain hardening are shown to be a consequence of atomic scale processes.

A new thermal non-contact mode of AFM operation based on the thermal noise response of the cantilever is demonstrated. The separation dependent tip-sample interactions change the resonant frequency of the cantilever. This fact is used to maintain a constant tip-sample separation by the feedback of the resonant frequency. In this frequency modulation technique the cantilever's thermal noise

response is used to estimate the changes in the resonance. This eliminates the need for a positive feed-back and allows for the operation at room temperatures without externally exciting the cantilever. In the experiments performed in ambient room conditions, tip-sample separations as small as 1.5 nm are achieved for time periods in excess of 30 mins. At such small separations a narrowband signal at 250 Hz is imaged with a force sensitivity of 14 fN in a bandwidth of 0.4 Hz. Therefore this technique is particularly suited for studying highly localized slowly evolving atomic or molecular scale phenomena at ambient temperatures.

In its current state thermal non-contact AFM is severely limited in bandwidth due to a large vari-ance in the frequency estimates. To improve the bandwidth, sensitivity and resolution, better frequency estimation methodologies need to be explored [113]. Recursive algorithms lend themselves naturally to applications dealing with frequency tracking. The Kalman filter is one such powerful adaptive method that has been used for frequency estimation elsewhere [114, 115]. Recently, a recursive Pisarenko harmonic decomposition (PHD) algorithm for single-tone frequency tracking has been shown to per-form better than the ordinary PHD [116]. One ideal application of thermal non-contact mode AFM is in studying biomolecular interactions that have large time scales on the order of a few milliseconds. Since such studies are almost always in liquid where the cantilever damping is severe, the advanced frequency estimation methods will be especially useful. In this small amplitude technique extremely stiff cantilevers are mandated to explore the complete tip-sample interaction potential. However, stiffer cantilevers have smaller thermal fluctuations that would require ultra low noise displacement sensors. Alternatively white noise driven cantilevers [117] can be used. Another interesting alternative is to use cantilever suspended perpendicular to the sample surface like a pendulum [118]. In this configuration extremely soft cantilevers can be used without any jump-to-contact instability.

The theoretical investigations in this thesis demonstrate their relevance in gaining insights into the experimentally observed phenomena in material deformation. Advances in computational software and hardware are making the study of large scale systems manageable. At the same time new experimental techniques in SPM are demonstrating the ability to probe and manipulate extremely small regions of matter. The narrowing gap between the length scales being investigated by computer simulations and laboratory experiments makes a complementary approach an ideal one.

BIBLIOGRAPHY

[1] R. Feynman, "There's Plenty of Room at the Bottom," 1959.

[2] G. Binning, C. F. Quate, and C. Gerber, "Atomic force microscope," *Phys. Rev. Lett.*, vol. 56, pp. 930, 1986.

[3] H. C. Hoch, L. W. Jelinski, and H. G. Craighead, Eds., *Nanofabrication and Biosystems: Integrating Materials Science, Engineering, and Biology*, Cambridge University Press, Cambridge [UK]; New York, 1996.

[4] M Benoit, D. Gabriel, G. Gerisch, and H. E. Gaub, "Discrete interactions in cell adhesion measured by single-molecule force spectroscopy," *Nat. Cell. Biol.*, vol. 2, pp. 313, 2000.

[5] U. Dammer, M. Hegner, D. Anselmetti, P. Wagner, M Drier, W. Huber, and H. J. Guntherodt, "Specific antigen/antibody interactions measured by force microscopy," *Biophys. J.*, vol. 70, pp. 2437, 1996.

[6] J. Fritz, M. K. Baller, H. P. Lang, H. Rothuizen, P. Vettiger, E. Meyer, H. J. Gntherodt, Ch. Gerber, and J. K. Gimzewski, "Translating biomolecular recognition into nanomechanics," *Science*, vol. 288, pp. 316, 2001.

[7] D. Rugar, C. S. Yannoni, and J. A. Sidles, "Mechanical detection of magnetic resonance," *Nature*, vol. 360, pp. 563, 1992.

[8] J. A. Sidles, "Folded stern-gerlach experiment as a means for detecting nuclear magnetic resonance in individual nuclei," *Phys. Rev. Lett.*, vol. 68, pp. 1124, 1992.

[9] K. Holczer, "Development of a single electron spin microscope," DARPA, MOSAIC Proposal, 2001.

[10] R. Wiesendanger, *Scanning Probe Microscopy and Spectroscopy*, Cambridge University Press, 1998.

[11] G. Binning and H. Rohrer, "Scanning tunnelling microscopy," *Helv. Phys. Acta*, vol. 55, pp. 726, 1982.

[12] G. Binning, Ch. Gerber, E. Stoll, T. R. Albrecht, and C. F. Quate, "Atomic resolution with atomic force microscopy," *Europhys. Lett.*, vol. 3, pp. 1281, 1987.

[13] P. K. Hansma, V. B. Elings, O. Marti, and C. E. Bracker, "Scanning tunneling microscopy and atomic force microscopy: Application to biology and technology," *Science*, vol. 242, pp. 209, 1988.

[14] G. Meyer and N. M. Amer, "Optical-beam-deflection atomic force microscopy: The NaCl (001) surface," *App. Phys. Lett.*, vol. 56, pp. 2100, 1990.

[15] R. García and R. Pérez, "Dynamic atomic force microscopy methods," *Surf. Sci. Rep.*, vol. 47, pp. 197, 2002.

[16] E. Meyer, H. J. Hug, and R. Benneewitz, *Scanning Probe Microscopy: The Lab on a Tip*, Springer, Heidelberg, 2004.

[17] S. Morita, R. Wiesendanger, and E. Meyer, Eds., *Noncontact Atomic Force Microscopy*, NanoScience and Technology. Springer, Berlin, 2002.

[18] G. Meyer and N. M. Amer, "Novel optical approach to atomic force microscopy [Appl. Phys. Lett. 53, 1045 (1988)]," *Appl. Phys. Lett.*, vol. 53, no. 24, pp. 2400, 1988.

[19] D. Rugar, H. J. Mamin, and P. Günther, "Improved fiber optic interferometer for atomic force microscopy," *App. Phys. Lett.*, vol. 55, pp. 2588, 1989.

[20] D. Sarid, D. Iams, V. Weissenberger, and L. S. Bell, "Compact scanning force microscope using a laser diode," *Opt. Lett.*, vol. 13, pp. 1057, 1988.

[21] R. C. Barrett, M. Tortonese, and C. F. Quate, "Atomic resolution with an atomic force microscope using piezoresistive detection," *App. Phys. Lett.*, vol. 62, pp. 834, 1993.

[22] D. Rugar, H. J. Mamin, R. Erlandsson, J. E. Stern, and B. D. Terris, "Force microscope using a fiber-optic displacement sensor," *Rev. Sci. Instrum.*, vol. 59, no. 11, pp. 2337, November 1988.

[23] M. Radmacher, J. P. Cleveland, and P. K. Hansma, "Improvement of thermally induced bending of cantilevers used for afm," *Scanning*, vol. 17, no. 2, pp. 117, 1995.

[24] M. B. Viani, T. E. Schäffer, and A. Chand, "Small cantilevers for force spectroscopy of single molecules," *J. App. Phys.*, vol. 86, no. 14, pp. 2258, August 1999.

[25] D. Tabor and R. H. S. Winterton, "Direct measurement of normal and retarted van der Waals forces," *Pro. R. Soc. London, Ser. A*, 1969.

[26] G. M. McClleland, R. Erlandsson, and C. Chiang, "Atomic force microscopy: General principles and a new implementation," *Rev. Prog. Quant. Nondestr. Eval.*, vol. 6B, pp. 1307, 1987.

[27] Y. Martin, C. C. Williams, and H. K. Wickramasinghe, "Atomic force microscope-force mapping and profiling on a sub 100-åscale," *J. App. Phys.*, vol. 61, no. 10, pp. 4723, May 1987.

[28] T. R Albrecht, P. Grütter, D. Horne, and D. Rugar, "Frequency-modulation detection using high-q cantilevers for enhanced force microscope sensitivity," *J. App. Phys.*, vol. 69, no. 2, pp. 668, January 1991.

[29] F. J. Giessibl, "Advances in atomic force microscopy," *Rev. Mod. Phys.*, vol. 75, no. 3, pp. 949, July 2003.

[30] Zhong Q., D. Innis, K. Kjoller, and V. B. Elings, "Fractured polymer silica fiber surface studied by tapping mode atomic-force microscopy," *Surf. Sci.*, vol. 290, pp. L688, 1993.

[31] R. Erlandsson, L. Olsson, and P. Martensson, "Inequivalent atoms and imaging mechanisms in ac-mode atomic-force microscopy of Si(111)(7 × 7)," *Phys. Rev. B*, vol. 54, no. R8309, 1997.

[32] P. K. Hansma, J. P. Cleveland, M. Radmacher, D. A. Walters, P. E. Hillmer, M. Bezanilla, M. Fritz, D. Vie, H. G. Hansma, C. B. Prater, J. Massie, L. Fukunaga, J. Gurley, and V. Elings, "Tapping mode atomic force microscopy in liquids," *App. Phys. Lett.*, vol. 64, pp. 1738, 1994.

[33] C. A. J. Putman, K. O. van der Werf, B. G. De Gooth, N. F. Van Hulst, and J. Greve, "Tapping mode atomic force microscopy in liquid," *App. Phys. Lett.*, vol. 64, no. 18, pp. 1454, 1994.

[34] F. J. Giessibl, "Atomic resolution of the silicon (111)-(7 × 7) surface by atomic force microscopy," *Science*, vol. 267, pp. 68, 1995.

[35] Franz J. Giessibl and Hartmut Bielefeldt, "Physical interpretation of frequency-modulation atomic force microscopy," *Phys. Rev. B*, vol. 61, no. 15, pp. 9968, April 2000.

[36] F. J. Giessibl, "A direct method to calculate tip-sample forces from frequency shifts in frequency-modulation atomic force microscopy," *App. Phys. Lett.*, vol. 78, pp. 123, 2001.

[37] U. Dürig, "Extracting interaction forces and complementary observables in dynamic probe microscopy," *App. Phys. Lett.*, vol. 76, pp. 1203, 2000.

[38] F. J. Giessibl, H. Bielefeldt, S. Hembacher, and J. Mannhart, "Calculation of the optimal imaging parameters for frequency modulation atomic force microscopy," *Appl. Surf. Sci.*, vol. 140, pp. 352, 1999.

[39] F. J. Giessibl, H. Bielefeldt, S. Hembacher, and J. Mannhart, "Imaging of atomic orbitals with the atomic force microscope - Experiments and simulations," *Ann. Phys. (Leipzig)*, vol. 10, pp. 887, 2001.

[40] P. M. Hoffmann, S. Jeffery, J. B. Pethica, H. Ö. Özer, and A. Oral, "Energy dissipation in afm and atomic loss processes," *Phys. Rev. Lett.*, vol. 87, pp. 265502, 2001.

[41] P. M. Hoffmann, A. Oral, R. A. Grimble, H. Ö. Özer, S. Jeffery, and J. B. Pethica, "Direct measurement of interatomic force gradients using an ultra-low-amplitude atomic force microscope," *Proc. R. Soc. Lond. A*, vol. 457, pp. 1161, 2001.

[42] P. M. Hoffmann, S. Jeffery, A. Oral, R. A. Grimble, H. Ö. Özer, and J. B. Pethica, "Nanomechanics using an ultra-small amplitude afm," *Mat. Res. Soc. Symp. Proc.*, vol. 649, pp. Q9.2 1, 2001.

[43] D. R. Sahoo, A. Sebastian, , and M. V. Salapaka, "Transient-signal-based sample-detection in atomic force microscopy," *App. Phys. Lett.*, vol. 83, no. 26, pp. 5521, December 2003.

[44] S. G. Corcoran, R. J. Colton, E. T. Lilleodden, and W. W. Gerberich, "Anomalous plastic deformation at surfaces: Nanoindentation of gold single crystals," *Phys. Rev. B*, vol. 55, no. 24, pp. R16057, June 1997.

[45] J. D. Kiely and J. E. Houston, "Nanomechanical properties of Au(111), (001) and (110) surfaces," *Phys. Rev. B*, vol. 57, no. 19, pp. 12588, May 1998.

[46] J. D. Kiely, K. F. Jarausch, J. E. Houston, and P. E. Russell, "Initial stages of yield in nanoindentation," *J. Mater. Res.*, vol. 14, no. 6, pp. 2219, June 1999.

[47] A. R. Leach, *Molecular Modelling : Principles and Applications*, Addison Wesley and Longman Ltd., Essex, 1996.

[48] M. Allen and D. Tildesley, *Computer Simulation of Liquids*, Clarendon Press, Oxford, 1987.

[49] D. Frenkel and B. Smit, *Understanding Molecular Simulation: From Algorithms to Applications*, vol. 1 of *Computational Science Series*, Academic Press, New York, 2 edition, 2002.

[50] F. H. Stillinger and T. A. Weber, "Computer simulation of local order in condensed phases of silicon," *Phys. Rev. B*, vol. 31, pp. 5262, 1985.

[51] Y. Kimura, Y. Qi, T. Çağin, and W. A. Goddard III, "The quantum Sutton-Chen many-body potential for properties of fcc metals," Unpublished, July 1998.

[52] A. P. Sutton and J. Chen, "Long-range finnis-sinclair potentials," *Philos. Mag. Lett.*, vol. 61, pp. 139, 1990.

[53] U. Landman, W. D. Luedtke, N. A. Burnham, and R. J. Colton, "Atomistic mechanisms and dynamics of adhesion, nanoindentation, and fracture," *Science*, vol. 248, pp. 454, 1990.

[54] J. S. Kallman, W. G. Hoover, C. G. Hoover, A. J. De Groot, S. M. Lee, and F. Wooten, "Molecular dynamics of silicon indentation," *Phys. Rev. B*, vol. 47, pp. 7705, 1993.

[55] D. W. Brenner, S. B. Sinnott, J. A. Harrison, and O. A. Shenderova, "Simulated engineering of nanostructures," *Nanotechnology*, vol. 7, pp. 161, 1996.

[56] A. Buldum, S. Ciraci, and I. P. Batra, "Contact, nanoindentation, and sliding friction," *Phys. Rev. B*, vol. 57, pp. 2468, 1998.

[57] C. L. Kelchner, S. J. Plimpton, and J. C. Hamilton, "Dislocation nucleation and defect structure during surface indentation," *Phys. Rev. B*, vol. 58, no. 17, pp. 11085, November 1998.

[58] W. C. D. Cheong and L. C. Zhang, "Molecular dynamics simulation of phase transformations in silicon monocrystals due to nano-indentation," *Nanotechnology*, vol. 11, pp. 173, 2000.

[59] R. Pérez, M. C. Payne, and A. D. Simpson, "First principles simulations of silicon nanoindentation," *Phys. Rev. Lett.*, vol. 75, pp. 4748, 1995.

[60] R. Astala, M. Kaukonen, R. M. Nieminen, and T. Heine, "Nanoindentation of silicon surfaces: Molecular-dynamics simulations of atomic force microscopy," *Phys. Rev. B*, vol. 61, pp. 2973, 2000.

[61] W. Smith and T. R. Forester, "DL_POLY is a package of molecular simulation routines," 1996, © The Council for the Central Laboratory of the Research Councils, Daresbury Laboratory at Daresbury, Nr, Warrington.

[62] W. D. Luedtke, ," Private Communication, 1998.

[63] G Dieter, *Mechanical Metallurgy*, McGraw-Hill, New York, 1967.

[64] T. Egami and J. Srolovitz, "Local structural fluctuations in amorphous and liquid metals: A simple theory of glass transition," *J. Phys. F*, vol. 12, pp. 2141, 1982.

[65] M. L. Falk and J. S. Langer, "Dynamics of viscoplastic deformation in amorphous solids," *Phys. Rev. E*, vol. 57, pp. 7192, 1998.

[66] W. D. Luedtke and U. Landman, "Preparation and melting of amorphous silicon by molecular-dynamics simulations," *Phys. Rev. B*, vol. 37, pp. 4656, 1988.

[67] D. R. Clarke, M. C. Kroll, P. D. Kirchner, R. F. Cook, and B. J. Hockey, "Amorphization and conductivity of silicon and germanium induced by indentation," *Phys. Rev. Lett.*, vol. 60, pp. 2156, 1988.

[68] T. F. Page, W. C. Oliver, and C. J. McHargue, "The deformation-behavior of ceramic crystals subjected to very low load (nano)indentations," *J. Mater. Res.*, vol. 7, pp. 450, 1992.

[69] G. M. Pharr, W. C. Oliver, and S. Harding, "New evidence for a pressure induced phase transformation during the indentation of silicon," *J. Mater. Res.*, vol. 6, pp. 1129, 1991.

[70] E. R. Weppelmann, J. S. Field, and M. V. Swain, "Observations, analysis, and simulation of the hysteresis of silicon using ultra-microindentation with spherical indenters," *J. Mater. Res.*, vol. 8, pp. 830, 1993.

[71] T. Suzuki and T. Ohmura, "Ultra-microindentation of silicon at elevated temperatures," *Phil. Mag. A*, vol. 74, pp. 1073, 1996.

[72] G. S. Smith, E. B. Tadmor, and E. Kaxiras, "Multiscale simulation of loading and electrical resistance in silicon nanoindentation," *Phys. Rev. Lett.*, vol. 84, pp. 1260, 2000.

[73] K. J. Chang and M. L. Cohen, "Solid-solid phase transitions and soft phonon modes in highly condensed Si," *Phys. Rev. B*, vol. 31, pp. 7819, 1985.

[74] J. Z. Hu, L. D. Merkle, C. S. Menoni, and I. L. Spain, "Crystal data for high-pressure phases of silicon," *Phys. Rev. B*, vol. 34, pp. 4679, 1986.

[75] A. B. Mann, D. van Heerden, J. B. Pethica, and T. P. Weihs, "Size dependent phase transformations during point-loading of silicon," *J. Mater. Res.*, vol. 15, pp. 1754, 2000.

[76] K. Minowa and K. Sumino, "Stress-induced amorphization of silicon crystal by mechanical scratching," *Phys. Rev. Lett.*, vol. 69, pp. 320, 1992.

[77] S. Mader, A. Seeger, and H. M. Thieringer, "," *J. Appl. Phys.*, vol. 34, pp. 3376, 1963.

[78] M. S. Whelan, "," in *The Physics of Metals: Defects*, P. B. Hirsch, Ed., vol. 2, p. 98. Cambridge University, London, 1975.

[79] R. A. Wind, Martin J. Murtagh, F. Mei, Y. Wang, M. A. Hines, and S. L. Sass, "Fabrication of nanoperiodic surface structures by controlled etching of dislocations in bicrystals," *Appl. Phys. Lett*, vol. 78, no. 15, pp. 2205, April 2001.

[80] J. A. Zimmerman, C. L. Kelchner, P. A. Klein, J. C. Hamilton, and S. M. Foiles, "Surface step effects on nanoindentation," *Phys. Rev. Lett.*, vol. 87, no. 16, pp. 165507, October 2001.

[81] M. F. Horstemeyer and M. I. Baskes, "Strain tensors at the atomic scale," in *Multiscale Phenomena in Materials - Experiments and Modeling*, I. M. Robertson, D. H. Lassila, B. Devincre, and R. Phillips, Eds., Pennsylvania, 2000, vol. 578 of *Materials Research Society Symposium Proceedings*, p. 15, Materials Research Society.

[82] E. Schmid and W. Boas, *Crystal Plasticity*, Hughes and Co. Ltd., London, 1950.

[83] A. Gannepalli and S. K. Mallapragada, "Molecular dynamics studies of plastic deformation during silicon nanoindentation," *Nanotechnology*, vol. 12, pp. 250, August 2001.

[84] K. L. Johnson, *Contact Mechanics*, Cambridge University Press, Cambridge, 1985.

[85] X. J. Ning and N. Huvey, "Observation of twins formed by gliding of successive surface-nucleated partial dislocations in silicon," *Philos. Mag. Lett*, vol. 74, pp. 241, 1996.

[86] J. Doerschel, "Transmission electron-microscope investigation of indentation induced dislocation configurations on the (001) GaSb face," *Z. Kristallogr.*, vol. 209, pp. 210, 1994.

[87] S. V. Kamat and J. P. Hirth, "Dislocation injection in strained multilayer structures," *J. Appl. Phys.*, vol. 67, pp. 6844, 1990.

[88] H. Gao, "Some general properties of stress-driven surface evolution in a heteroepitaxial thin film structure," *J. Mech. Phys. Solids*, vol. 42, pp. 741, 1994.

[89] G. E. Beltz and L. B. Freund, "Dislocation emission at surfaces," in *Thin Films: Stresses and Mechanical Properties V*, S. P. Baker, P. Borgesen, P. H. Townsend, C. A. Ross, and C. A. Volkert, Eds., Pennsylvania, 1995, vol. 356 of *Materials Research Society Symposium Proceedings*, p. 93, Materials Research Society.

[90] J. Zou and J. H. Cockayne, "Nucleation of semicircular misfit dislocation loops from the epitaxial surface of strained-layer heterostructures," *J. Appl. Phys.*, vol. 79, pp. 7632, 1996.

[91] ," The Schmid factors for $\sigma = \sigma_{zz}$ on (111) along $[10\bar{1}]$, $[01\bar{1}]$ and $[11\bar{2}]$ are 0.4082, 0.4082 and 0.4714 respectively.

[92] V. Vitek, "Intrinsic stacking faults in body-centered cubic crystals," *Phil. Mag.*, vol. 18, pp. 773, 1968.

[93] V. Vitek, L. Lejcek, and D. K. Bowen, "On the factors controlling the structure of the dislocation cores in bcc crystals," in *Interatomic Potentials and Simulation of Lattice Defects*, P. C. Gehlen, J. R. Beeler Jr, and R. L. Jaffee, Eds., New York, 1972, p. 493, Plenum Press.

[94] J. R. Rice, "Dislocation nucleation from a crack tip: An analysis based on the Peierls concept," *J. Mech. Phys. Solids*, vol. 40, no. 2, pp. 239, 1992.

[95] R. von Mises, ," *Z. Angew. Math. Mech.*, vol. 8, pp. 161, 1928.

[96] G. W. Groves and A. Kelly, "Independent slip systems in crystals," *Phil. Mag.*, vol. 8, pp. 877, 1963.

[97] J. F. W. Bishop, "A theoretical examination of the plastic deformation of crystals by glide," *Phil. Mag.*, vol. 42, pp. 414, 1953.

[98] C. N. Reid, *Deformation Geometry for Materials Scientists*, vol. 11 of *International Series on Materials Science and Technology*, Pergamon Press, Oxford, 1973.

[99] J. F. W. Bishop and R. Hill, "A theory of the plastic distortion of a polycrystalline aggregate under combined stresses," *Phil. Mag.*, vol. 42, pp. 414, 1951.

[100] J. F. W. Bishop and R. Hill, "A theoretical derivation of the plastic properties of a polycrystalline face-centered metal," *Phil. Mag.*, vol. 42, pp. 1298, 1951.

[101] R. Eckert, S. Jeney, and J. K. H. Hörber, "Understanding intercellular interactions and cell adhesion: Lessons from studies on protein-metal interactions," *Cell Biol. Int.*, vol. 21, no. 11, pp. 707, November 1997.

[102] A. Razatos, Y-L. Ong, M. M. Sharma, and G. Georgiou, "Molecular determinants of bacterial adhesion monitored by atomic force microscopy," *Proc. Natl. Acad. Sci.*, vol. 95, pp. 11059, September 1998.

[103] M. Stolz, D. Stoffler, U. Aebi, and C. Goldsbury, "Monitoring biomolecular interactions by time-lapse atomic force microscopy," *J. Struct. Biology*, vol. 131, pp. 171, 2000.

[104] M. Mondon, S. Berger, and C. Ziegler, "Scanning-force techniques to monitor time-dependent changes in topography and adhesion force of proteins on surfaces," *Anal. Bioanal. Chem.*, vol. 375, pp. 849, 2003.

[105] F. J. Giessibl, S. Hembacher, H. Bielefeldt, and J. Mannhart, "Subatomic features on the silicon (111)-(7×7) surface observed by atomic force microscopy," *Science*, vol. 289, pp. 422, July 2000.

[106] F. J. Giessibl, "Atomic force microscopy in ultrahigh vacuum," *Jpn. J. Appl. Phys. Part I*, vol. 33, no. 6B, pp. 3726, 1994.

[107] J. E. Sader, "Frequency response of cantilever beams immersed in viscous fluids with applications to the atomic force microscope," *J. App. Phys.*, vol. 84, pp. 64, 1998.

[108] H. Stark and J. W. Woods, *Probability, Random Processes and Estimation Theory for Engineers*, Prentice Hall, Englewood NJ, 1994.

[109] M. V. Salapaka, H. S. Bergh, J. Lai, A. Majumdar, and E. McFarland, "Multi-mode noise analysis of cantilevers for scanning probe microscopy," *J. App. Phys.*, vol. 81, no. 6, pp. 2480, March 1997.

[110] V. F. Pisarenko, "The retrieval of harmonics from a covariance function," *Geophysics. J. Roy. Astron. Soc.*, vol. 33, pp. 347, 1973.

[111] U. Dürig, O. Züger, and A. Stalder, "Interaction force detection in scanning probe microscopy: Methods and applications," *J. App. Phys.*, vol. 72, no. 5, pp. 1778, September 1992.

[112] F. J. Giessibl, *Noncontact Atomic Force Microscopy*, chapter Principle of NC-AFM, p. 11, NanoScience and Technology. Springer, Berlin, 2002.

[113] B. G. Quinn and E. J. Hannan, *The Estimation and Tracking of Frequency*, Cambridge Series in Statistical and Probabilistic Mathematics. Cambridge University Press, Cambridge, UK, 2001.

[114] P.Y. Kam, L. C. Teong, and C. C. See, "Frequency offset estimation via planar extended kalman filter," *Electron. Lett.*, vol. 29, pp. 1473, 1993.

[115] A. Routray, A. K. Pradhan, and K. P. Rao, "A novel kalman filter for frequency estimation of distorted signals in power systems," *IEEE T. Instrum. Meas.*, vol. 51, pp. 469, 2002.

[116] H. C. So, "A comparative study of three recursive least-squares algorithms for single-tone frequency tracking," *Signal Processing*, vol. 83, pp. 2059, 2003.

[117] D. O. Koralek, W. F. Heinz, M. D. Antonik, A. Baik, and J. H. Hoh, "Probing deep interaction potentials with white-noise-driven atomic force microscope cantilevers," *IEEE T. Instrum. Meas.*, vol. 76, pp. 2952, 2000.

[118] H. J. Mamin, R. Budakian, B. W. Chui, and D. Rugar, "Detection and manipulation of statistical polarization in small spin ensembles," *Phys. Rev. Lett.*, vol. 91, pp. 207604, 2003.